CORRECTION AND SCOPE

A Ward-Completed Compact Spin-2 Carrier with Tower-Filtered Finite-Spin Spectra

The response carrier is an effective construction. The finite-spin spectra come from reduced boxes. Fits across L = 3–5 gave about 0.354, 0.402 and −0.681 against targets 1, 1 and −2.

Manuscript · p. 1, version 4.1

Tower-Filtered ED Lanczos Scaling Audit for the Compact Ward-Square Spin-2 Box

Evidence · Reduced finite-spin tower scaling / One-Hamiltonian composition requirements

A Ward-Completed Compact Spin-2 Carrier with Tower-Filtered Finite-Spin Spectra

QATNU Project Draft

Version 4.1 – July 3, 2026

Abstract

We construct and audit a local first-class spin-2 response architecture organized around a four-face locality obstruction: compact finite-dimensional tensor characters generically give a $z = 3$ phase, exact local TT sources are Cotton suppressed, first-classness alone does not protect a massless pole, and a lone periodic bulk cone violates topological charge conservation. The construction pays these debts in stages. A finite synthetic-domain-wall carrier pays the doubling debt by separating an origin node of charge $+1$ from a mirror node of charge -1. A positive local chiral bosonic stiffness

$$K_{\mathrm{ch}}(k) = D(k)^{\dagger} D(k) + \|n(k)\|^2 I$$

then avoids the branch doubling of the naive square lift and gives one scalar boundary oscillator; tensoring with the exact first-class TT quotient gives exactly two positive spin-2 branches. The continuous-variable/Gaussian carrier has $z = 0.999786593981$, finite boundary residue, a gapped second scalar branch, exact first-class residuals below 4×10^{-16}, and projected/conserved-source response $\chi_{\mathrm{TT}}(0, k) \sim k^{-2}$.

The paper then records the later finite-dimensional and matter-coupling upgrades. A Ward-completed dynamical stress sector replaces an unprotected hS coupling by the positive local covariant square

$$H_m = \frac{\Omega^2}{2} \|S - \alpha h_{\mathrm{wall}}\|^2,$$

fixing the seagull by an exact diagonal shift symmetry. The coupled effective model retains exactly two low TT branches, $z_1 = 0.999606677871$, $z_2 = 0.999541049078$, and Ward-stress response $\chi_S(0, k) \sim k^{-1.999574909721}$. The remaining seagull locality problem is resolved at the harmonic local-constraint level by promoting the relative field $R = S - \alpha A$ and imposing local constraints $\nabla_i R_{ij} = 0$ and $\mathrm{tr}\, R = 0$: the TT projector is recovered only by constraint elimination, Coulomb-style, not inserted as a microscopic kernel. The assembled full tensor/matter hard-constrained symbol has 102 coordinates and 68 constraint rows for $W = 16$, constrained dimension $34 = 2W + 2$, two low branches with $z_1 = 0.999999525$, $z_2 = 0.999999518$, Ward response exponent -1.997024224, and a third gap near 0.184536746.

Compact and finite-spin tests now substantially sharpen the claim. The simple compact profile $r_0 = 1$ avoids the charge hierarchy of localized rational locks, keeps $N_{\mathrm{low}} = 2$, $z \simeq 1$, $\chi_S(0, k) \sim k^{-2}$, residue $Z_S = 1/(W + 1) = 1/17$, and a finite second gap. Diagonal 3D XY Monte Carlo confirms an ordered compact $U(1)$ sector with finite helicity stiffness and vortex suppression. Full compact tensor/matter screens remain ordered, hard-constrained quotient screens show no extra zero on the audited Brillouin grid, and finite-spin saturation is controlled by a bounded local spin-wave density $\bar{n}_{\max,\infty} \simeq 0.0208$. Finally, a genuine finite-dimensional compact quantum box - an $L = 3$ ring times a minimal matter/tensor chain with truncated rotors $|n| \le J$ - shows the expected Anderson tower, a rapidly convergent magnon branch $\omega(2\pi/3) = 0.80484, 0.74001, 0.73890, 0.73888$ for $J = 1, 2, 3, 4$, and a finite matter-operator pole fraction converging to 0.4306, close to the box Debye-Waller prediction 0.416. A tower-filtered dynamic-structure audit separates the $Q = 1, k = 0$ Anderson tower from the finite-momentum source pole: at $k = 2\pi/3$ the tower is absent by momentum, the $J = 4$ pole lies at $\omega = 0.73888$ with pole fraction 0.4306, and the captured spectral window is about 0.946. The result

is therefore no longer only an effective CV carrier: it has a compact-rotor finite-spin route, hard-constrained spectral support, and a finite-spin quantum-box validation with an explicit tower-filtered spectral observable. It is still not a theorem-level proof of a full nonperturbative 3D finite-local-dimension graviton phase; the remaining step is a thermodynamic finite-spin gauge-Hamiltonian or transfer-matrix/QMC spectral proof for the full compact tensor/matter model.

Contents

1 Purpose and current claim boundary **2**
- 1.1 One obstruction, four faces . . . 2
- 1.2 Main result . . . 3

2 Route ledger: what was closed before the chiral lift **3**

3 Doubler conservation law: why the wall is required **5**

4 First-class Stueckelberg tensor quotient **7**

5 Single-cone signed carrier precursor **7**

6 Positive chiral bosonic lift **7**
- 6.1 Residue and branch isolation . . . 8
- 6.2 Locality and first-class closure . . . 9
- 6.3 Non-origin gaps . . . 10

7 Finite-depth Gaussian bosonic QCA realization **10**

8 Projected, auxiliary Ward, and local-source responses **11**

9 Ward-completed dynamical matter coupling **12**
- 9.1 Seagull uniqueness and stability . . . 14

10 Boundary-shift mass protection in the CV carrier **15**

11 Controlled finite-local-dimension truncation **17**
- 11.1 Finite-resource approximation laws . . . 18
- 11.2 Large-spin and finite-grid alternatives . . . 19

12 Why a simple protected fixed-d phase is still missing **20**
- 12.1 Trace obstruction for exact finite-dimensional CCR . . . 20
- 12.2 Onsite positive guard is relevant . . . 20
- 12.3 Global no-leakage versus local control . . . 21

13 Compact-rotor and finite-spin Ward-square route **21**

14 Local Ward-stress Gauss law and covariant seagull localization **23**

15 Full compact tensor/matter Ward-square target **25**

16 Hard constraints, finite spin, and compact phase screens **27**

17 Microscopic finite-spin quantum box **28**
17.1 Tower-filtered dynamic structure factor 29

18 Updated interpretation **30**

19 Next calculations **31**

20 Conclusion **31**

A Latest audit summary **32**

B Numerical audit summary **33**

C Companion internal reports **33**

1 Purpose and current claim boundary

This paper supersedes the earlier single-cone carrier draft and the first chiral-bosonic freeze by incorporating the positive chiral bosonic lift, the finite-local-dimension truncation audits, the conserved-source response audit, the CV mass-protection audit, the finite-resource approximation laws, the topological doubling analysis, and the new Ward-completed dynamical matter-coupling audit. The target is still deliberately narrower than full emergent gravity. We seek a local architecture whose constrained infrared sector contains exactly two transverse-traceless spin-2 branches with

$$\omega(k) = c_g\,|k| + \mathcal{O}(|k|^3), \qquad N_+(k) = 2, \qquad Z_{\rm local}(k \to 0) > 0, \tag{1}$$

whose projected or externally conserved TT response obeys

$$\chi_{\rm TT}(0,k) \sim \frac{1}{|k|^2}, \tag{2}$$

and whose constraints are propagated as an exact first-class system. The claim is not universal coupling, nonlinear diffeomorphism invariance, or native emergence from the minimal ladder Hamiltonian. The claim is a local linear spin-2 bosonic response-carrier architecture, plus controlled finite-dimensional regularizations for local low-energy observables.

The new status is:

$$\boxed{\begin{array}{c}\text{first-class quotient} \to \text{topological domain-wall single cone} \to \text{positive chiral bosonic lift} \\ \to \text{Ward-completed matter square} \to \text{hard local constraints} \to \text{compact finite-spin quantum box}\end{array}} \tag{3}$$

The remaining unsolved target is a theorem-level protected fixed-local-dimension microscopic many-body phase in the full thermodynamic tensor/matter Hilbert space. The current evidence now includes hard-constrained harmonic spectra, compact ordered-sector screens, finite-spin saturation bounds, and an exact small-volume finite-spin box, but these are still scoped screens rather than a final nonperturbative phase proof. This boundary is central to the interpretation of the result.

1.1 One obstruction, four faces

The route is best understood as a single locality obstruction appearing in four guises. In three spatial dimensions the first local polynomial operator that is simultaneously gauge invariant, symmetric, transverse, and traceless is Cotton order. Equivalently, low-derivative local variables do not provide an exact TT tensor without either a nonlocal projector, an independent Ward-constrained stress variable, or an additional boundary/topological construction. The four faces are:

1. **Compact character face.** Exact compact finite-dimensional local tensor characters begin at derivative orders that force the generic strict-centralizer phase to have $z = 3$, rather than the relativistic $z = 1$ target.

2. **Source face.** Independent local stress variables under a local Ward constraint $d_i S_{ij} = 0$ couple at full $1/k^2$ strength, but derivative-built conserved sources are suppressed: Beltrami-type sources give k^{+2} response and exact local gauge-invariant Cotton sources give k^{+4} response.

3. **Mass face.** First-classness by itself does not forbid a positive local mass term. Masslessness requires an additional Ward/Goldstone symmetry; in the effective construction this is the diagonal shift of the Ward-completed square.

4. **Doubler face.** A local periodic bulk symbol cannot carry one isolated cone of nonzero topological charge. The synthetic domain wall does not delete the opposite charge; it separates it onto the other boundary and gaps the unwanted boundary carrier.

The chiral construction pays these debts in different currencies. Continuous variables evade the exact finite-dimensional canonical obstruction; the domain wall pays the topological doubling debt; the Ward-completed square supplies the finite stress residue and symmetry-fixed seagull at the Gaussian level; and finite-dimensional truncations are controlled for local observables. The unpaid debt is microscopic: a finite-local-dimension gauge, rotor, or topological phase whose exact low-energy symmetry realizes the same Ward-completed square.

1.2 Main result

Let $n(k)$ be the local coined connection vector from the preceding spin-2 walk. The first step is a finite synthetic-domain-wall carrier that isolates one lower-boundary cone while preserving the Stueckelberg first-class tensor quotient. The second, decisive step is to avoid squaring the signed Hermitian carrier. Instead define the positive scalar stiffness

$$K_{\mathrm{ch}}(k) = D(k)^{\dagger} D(k) + \|n(k)\|^2 \, I. \tag{4}$$

The synthetic chiral operator is nearest-neighbor in the synthetic coordinate,

$$(D\psi)_s = \psi_{s+1} - r(k)\psi_s, \qquad s = 0, \ldots, W-2, \tag{5}$$

with a top boundary row

$$(D\psi)_{W-1} = c(k)\psi_{W-1}. \tag{6}$$

The audited profile is

$$r(k) = 0.42 + 2.5 m_W(k), \qquad c(k) = 2 m_W(k), \tag{7}$$

where

$$m_W(k) = \frac{1}{4}\left(3 - \cos k_x - \cos k_y - \cos k_z\right). \tag{8}$$

The scalar stiffness K_{ch} has exactly one soft positive boundary oscillator at the origin and a finite second gap. Tensoring that scalar oscillator with the two-dimensional TT quotient gives exactly two positive TT branches.

Table 1: Headline diagnostics for the chiral bosonic spin-2 lift.

Diagnostic	Value
Scalar IR exponent z	0.999786593981
Scalar prefactor	0.0996265850063
Scalar low branch count at $\lvert k\rvert = 10^{-3}$	1
Positive TT branch count at $\lvert k\rvert = 10^{-3}$	2
Left-wall residue at first IR sample	0.823599999974
Left-wall residue at largest IR sample	0.820966233676
Second scalar gap at origin	0.581548368134
Known coined-doubler lowest frequency	1.406362005908
Minimum random-scan gap outside $\lvert k\rvert > 0.75$	0.070775077483
Constraint-surface residual	3.832×10^{-16}
Gauge-surface residual	3.331×10^{-16}
Spatial Chebyshev range of stiffness	2
Synthetic range of stiffness	1
Gaussian-QCA quasienergy exponent	0.999784912034
Gaussian-QCA symplectic residual	2.220×10^{-16}
Static projected-source exponent	-1.999525292313
Mean TT pole residue diagnostic	0.823598022519
Protected perturbation pass count	64/64
Local cutoff ratio η	0.145968795677

2 Route ledger: what was closed before the chiral lift

The current architecture is meaningful because many more direct routes failed. Table 2 records the logic. The common pattern is that an exact $z = 1$ tangent can often be obtained after reduction, but locality, positivity, finite local dimension, branch count, or finite local residue is lost by the microscopic realization.

Table 2: Route ledger leading to the chiral bosonic architecture. "Positive" refers to the scoped intermediate property, not to a completed graviton phase.

Route	Positive output	Failure or boundary
Positive quadratic normalizer	Exact reduced DeWitt/Einstein parent with two $z = 1$ TT branches	Positive semidefinite normalizers of an Abelian first-class algebra collapse to the strict centralizer.
Projector Hamiltonian	Exact code-space projection is support-local after stabilizer twirling	Local projector blocks inherit the compact $z = 3$ character obstruction.
Fixed-prime Clifford QCA	Exact finite-range automorphism with the right real tangent	Finite-p local Pauli seeds generate arithmetic quasienergy combs, not robust multidimensional local poles.
Cotton prepotential	Exact Dirac reduction gives two TT modes and $1/k^2$ response	Compact Cotton dynamics gives $z = 3$; finite positive penalty gives $z = 2$ in the thermodynamic infrared.

Route	Positive output	Failure or boundary
Topological Cotton factorization	Onsite brackets factorize the derivative Cotton Berry form	Positive static completion with $1/k^2$ response has $z \geq 2$; signed parent remains non-positive before reduction.
Coined/connection spin-2 walk	Fixed-dimensional local spin-2 pole with finite bare onsite residue	Helicity $0, \pm 1$ sectors remain soft and a second spin-2 node appears; topological charge conservation makes an opposite partner mandatory for a local periodic bulk symbol.
Stueckelberg-coined Wilson target	Exact quotient removes lower helicities; reduced Wilson dispersion gaps the second node	The local Wilson mass is not first class unless TT-projected; the exact projector has an algebraic tail.
Dynamical Wilson fields	Local first-class Wilson gap is possible	The quotient expands to seven oscillator pairs; extra Stueckelberg/helicity sectors remain soft.
Wilson partner	Local first-class doubler gap is possible	The TT sector doubles: four positive branches rather than two.
Signed domain wall	Local first-class single-boundary carrier with two TT positive branches; the wall separates the $+1$ and -1 node charges	Signed-band/one-particle object, not yet a positive bosonic Hamiltonian.
Naive square bosonic lift	Positive, local, and linear	Squares both signs of the boundary carrier and gives four low TT oscillator branches.
Positive-band projection	Correct branch count formally	The projector has an algebraic nonlocal real-space kernel.
Chiral bosonic lift	Positive local Gaussian oscillator/QCA with exactly two TT branches	Continuous-variable exact model with projected/conserved-source response and boundary-shift protection; finite qudit versions are controlled approximations, not exact fixed-d phases.

3 Doubler conservation law: why the wall is required

The single-cone domain wall is not just a convenient engineering device. It is how a local periodic bulk symbol pays a topological conservation law. The coined connection walk defines a finite-range map

$$n : T^3 \to \mathbb{R}^3, \tag{9}$$

and isolated cones occur at zeros of $n(k)$. Around a simple zero k_a, the local charge is the degree of the Gauss map $\hat{n} : S^2 \to S^2$, equivalently the sign of the Jacobian determinant for a fixed orientation convention,

$$Q_a = \operatorname{sgn} \det \left(\frac{\partial n_i}{\partial k_j} \right)_{k=k_a} . \tag{10}$$

On the Brillouin three-torus the total isolated charge must vanish. This is the Nielsen–Ninomiya/Poincare–Hopf content relevant here: a lone local bulk cone cannot occur without a compensating partner or a boundary/nonlocal escape.

The audit of the coined spin-2 walk finds two nodes,

$$k_0 = (0, 0, 0), \qquad k_D = (1.681311464, 1.681311464, 1.681311464), \tag{11}$$

with $d \simeq 1$ and $n \simeq 0$ at both. Their Jacobians have the same singular values,

$$\sigma_1 = \sigma_2 = \sigma_3 = \sin(0.1) = 0.0998334, \tag{12}$$

but opposite orientation:

$$\det J(k_0) = +9.950108 \times 10^{-4}, \qquad \det J(k_D) = -9.950108 \times 10^{-4}. \tag{13}$$

A direct solid-angle degree computation gives the same opposite-pair conclusion, up to the overall orientation convention of the enclosing sphere. Thus the non-origin node is not a numerical accident or a poor parameter choice. It is the mirror charge demanded by locality and periodicity.

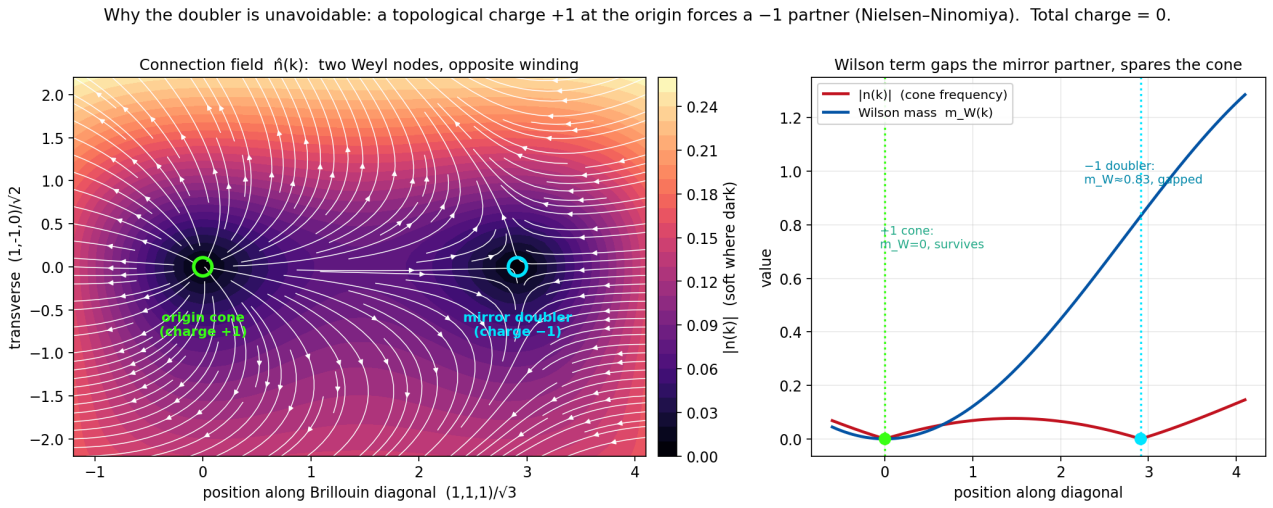

Figure 1: Topological reading of the coined connection walk. The origin cone and diagonal mirror node have opposite winding. The Wilson mass $m_W(k)$ vanishes at the origin and is $0.8327\ldots$ at the mirror node, so it spares the desired cone and gaps the partner in the domain-wall construction.

The Wilson scalar

$$m_W(k) = \frac{1}{4}\left(3 - \cos k_x - \cos k_y - \cos k_z\right) \tag{14}$$

obeys

$$m_W(k_0) = 0, \qquad m_W(k_D) = 0.8327177325. \tag{15}$$

The Wilson term cannot delete topological charge in the closed bulk. What the domain wall does instead is separate the two charges onto different synthetic boundaries, then select one wall. The upper-wall mass removes the mirror boundary carrier from the low-energy sector while the lower-wall cone remains. In this sense the synthetic wall is not one repair among many; under the assumptions of finite range, translation invariance, and a periodic bulk symbol, it is the clean local way to retain one cone without pretending that the compensating charge disappeared.

This observation also unifies several earlier failures. The square bosonic lift doubled branches because it treated both signed wall partners symmetrically. The Wilson-projection attempt removed the partner only by using a nonlocal TT projector. The successful route first pays the topological doubling debt at a boundary and only then constructs the positive chiral bosonic oscillator on the selected wall.

4 First-class Stueckelberg tensor quotient

The physical tensor variables are symmetric tensors A_{ij} and B_{ij} together with one Stueckelberg pair (ϕ, π). With six tensor components and the scalar pair, the real phase space has fourteen dimensions per spatial momentum. For a local connection vector $n(k)$, define

$$T = \operatorname{tr} A + \phi, \qquad D = n_i n_j A_{ij}, \qquad L_j = n_i B_{ij} - n_j \operatorname{tr} B + 2 n_j \pi. \tag{16}$$

The five constraints T, D, L_j are first class for nonzero $n(k)$.

Proposition 1 (First-class quotient)**.** *For nonzero $n(k)$, the constraints in Eq. (16) commute exactly and reduce the fourteen-dimensional real phase space to four physical real dimensions.*

Proof sketch. The coordinate constraints T, D commute with one another, and the momentum-type constraints L_j commute with one another. The trace–momentum bracket from $\operatorname{tr} A$ is canceled by the Stueckelberg bracket from $2 n_j \pi$. The scalar longitudinal bracket between D and L_j cancels between the $n_i B_{ij}$ and $-n_j \operatorname{tr} B$ terms. Hence the constraint matrix vanishes. Five first-class constraints remove ten real phase-space dimensions, leaving $14 - 2(5) = 4$ physical dimensions, i.e. two canonical pairs. □

This quotient is the mechanism that removes the helicity 0 and helicity ± 1 sectors. In the chiral bosonic construction the scalar copy/synthetic stiffness acts as the identity on this tensor quotient. Therefore first-classness is preserved before any boundary-mode selection.

5 Single-cone signed carrier precursor

Before the positive bosonic lift, the program constructed a finite synthetic-domain-wall signed carrier

$$H_{\mathrm{DW}}(k, s) = n_i(k) \Gamma_i + \left[M_0 + \beta m_W(k) + 1 \right] \Gamma_5 + \left(-\frac{1}{2} \Gamma_5 - \frac{i}{2} \Gamma_4 \right) T_s + \mathrm{h.c.}, \tag{17}$$

with

$$M_0 = -1, \qquad \beta = 10, \qquad W = 24, \qquad b_{\mathrm{top}} = 2. \tag{18}$$

The upper wall carries a local perturbation $b_{\mathrm{top}} \Gamma_1$. The lower wall hosts one positive carrier band; tensoring with the TT quotient yields two positive TT branches. The signed carrier had dispersion exponent

$$z = 0.999785606928, \tag{19}$$

unit-scale wall residue, first-class residuals below 7×10^{-16}, and no detected surviving non-origin cone in the audited deterministic and random scans. Its limitation was that it was a signed-band or one-particle carrier rather than a positive bosonic Hamiltonian.

A direct positive oscillator lift of H_{DW} used H_{DW}^2. This retained linearity, but converted both the positive and negative lower-wall partners into positive oscillator frequencies. After tensoring with the TT label, it produced four low TT branches. The chiral lift below was introduced to avoid that specific branch-doubling mechanism.

6 Positive chiral bosonic lift

The successful lift is not a square of the signed Hermitian carrier. It is a positive scalar stiffness built directly from a local chiral synthetic operator. The oscillator Hamiltonian is

$$H_{\mathrm{bos}} = \frac{1}{2} \sum_k \left(p(k)^\dagger p(k) + q(k)^\dagger K_{\mathrm{ch}}(k) q(k) \right). \tag{20}$$

With K_{ch} from Eq. (4), all eigenfrequencies are nonnegative by construction. The term $\|n(k)\|^2 I$ supplies the desired linear frequency after taking the square root of the stiffness eigenvalue. The chiral operator D supplies one lower-wall zero sector and a finite second scalar gap.

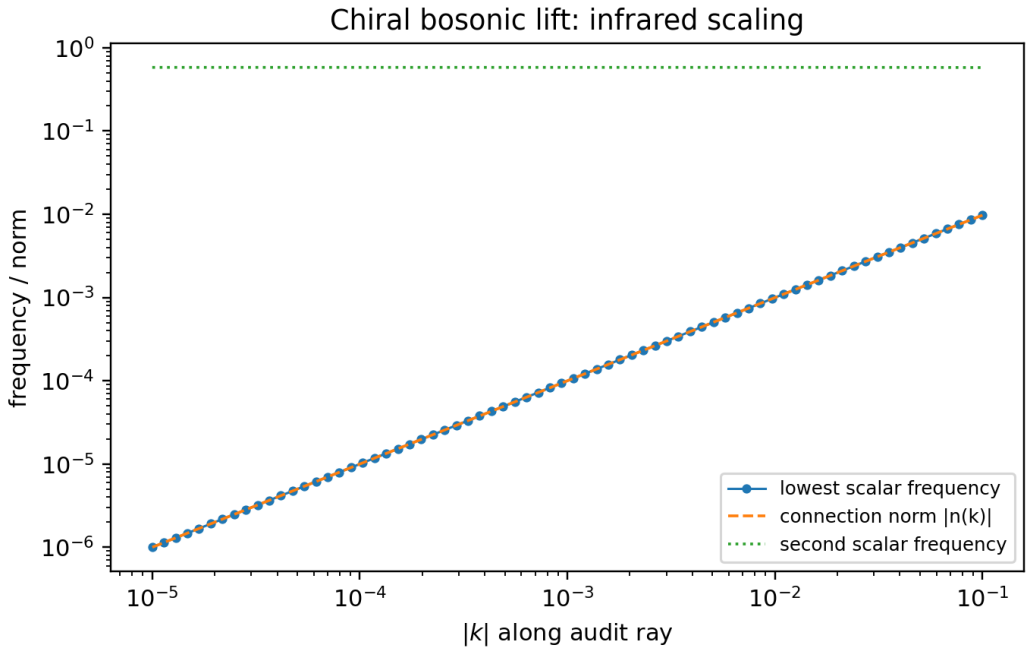

Figure 2: Infrared scaling of the chiral bosonic lift. The lowest scalar frequency tracks the connection norm $\|n(k)\|$, while the second scalar branch remains gapped.

Along the audited ray,

$$\omega_{\mathrm{low}}(k) = A\,|k|^{z}\,, \qquad z = 0.999786593981, \qquad A = 0.0996265850063, \tag{21}$$

with $R^2 = 0.999999970824$. The connection norm fit gives

$$z_n = 0.999785606959, \qquad A_n = 0.099625911259. \tag{22}$$

At $|k| = 10^{-3}$ there is one low scalar branch. Tensoring with the two TT polarizations gives exactly two positive TT branches.

6.1 Residue and branch isolation

The lower-wall oscillator has finite local residue. The first infrared sample gives

$$Z_{\mathrm{left}} = 0.823599999974, \tag{23}$$

and the largest audited infrared sample gives

$$Z_{\mathrm{left}} = 0.820966233676. \tag{24}$$

The right-wall weight is negligible in the same window. The second scalar gap at the origin is

$$\Delta_2(0) = 0.581548368134. \tag{25}$$

This is the key improvement over both the compact local-character constructions and the naive square lift. Compact exact local TT creators appeared first at high derivative order, suppressing residue. The square lift had residue but doubled the branch count. The chiral lift has finite boundary residue and one scalar branch.

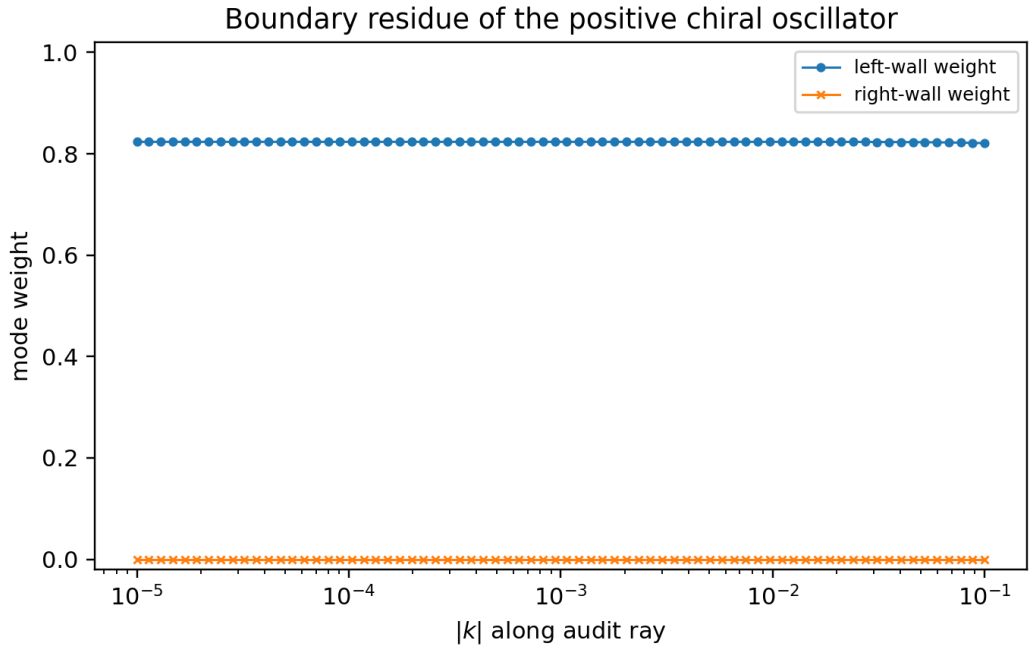

Figure 3: Boundary residue of the positive chiral oscillator. The lower-wall weight stays finite rather than derivative-suppressed.

6.2 Locality and first-class closure

The coefficients entering K_{ch} are finite trigonometric polynomials. The Fourier audit found spatial Chebyshev support within radius two, with only roundoff tails beyond that radius, and nearest-neighbor synthetic support. Representative coefficient ranges are summarized in Table 3.

Table 3: Locality audit for the chiral stiffness.

Function	Maximum coefficient	Support radius $> 10^{-12}$	Tail beyond radius 2
$\|n\|^2$	5.6092736×10^{-2}	2	3.58×10^{-18}
$r(k)$	2.295	1	5.04×10^{-17}
$r(k)^2$	5.8529625	2	2.64×10^{-16}
$c(k)$	1.5	1	3.63×10^{-17}
$c(k)^2$	2.625	2	5.90×10^{-17}

Because the scalar stiffness acts only in synthetic copy space and as identity on the Stueckelberg tensor quotient, it preserves the first-class ideal. The explicit nullspace audit gives

$$\|FKN_F\|_\infty = 3.8324546814910817 \times 10^{-16}, \tag{26}$$

$$\left\|N_G^\dagger KG\right\|_\infty = 3.3306690738754696 \times 10^{-16}, \tag{27}$$

with constraint-isotropy residual $1.8964542517715368 \times 10^{-19}$ and Hermiticity residual zero. The extended quotient dimension in the finite test was the expected 32.

6.3 Non-origin gaps

The known coined doubler is no longer soft in the chiral stiffness. At

$$k_D = (1.681311464, 1.681311464, 1.681311464), \tag{28}$$

one has

$$\|n(k_D)\| = 1.240971079080 \times 10^{-9}, \tag{29}$$

while the lowest chiral scalar frequency is

$$\omega_{\min}(k_D) = 1.406362005908. \tag{30}$$

The coarse grid scan outside the origin ball $|k| > 0.75$ found minimum gap 0.067271447003, and the 750-sample random scan found minimum gap 0.070775077483. As in the earlier audit, this is not an analytic proof that all accidental zeros are absent; it is the performed numerical node audit.

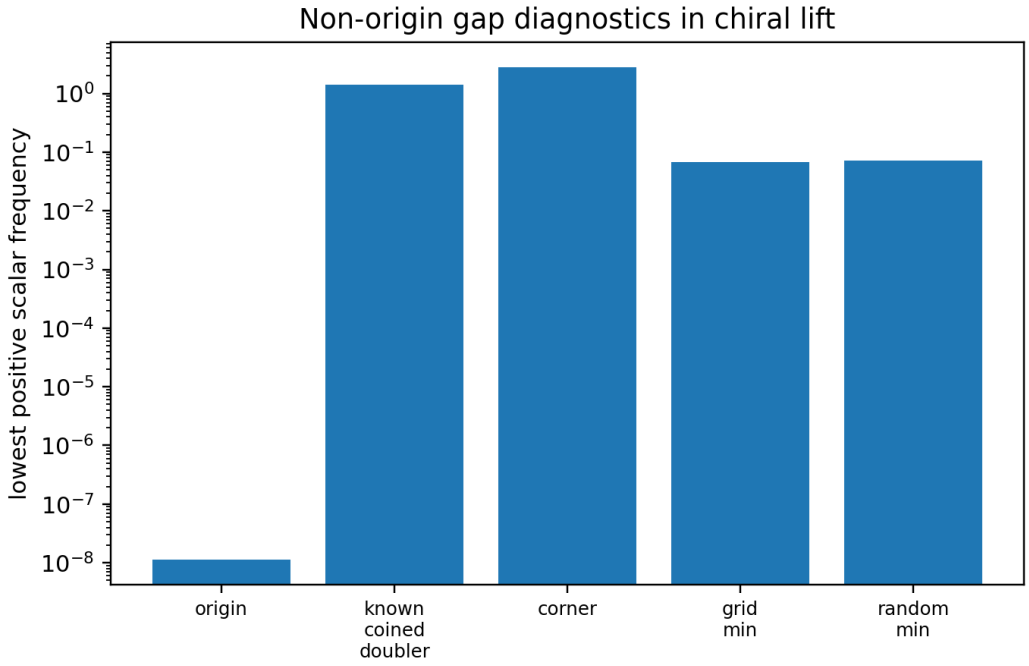

Figure 4: Non-origin gap diagnostics in the chiral lift. The known coined doubler is gapped even though $\|n(k_D)\|$ is essentially zero.

7 Finite-depth Gaussian bosonic QCA realization

The same positive stiffness admits a finite-depth Gaussian bosonic QCA through the three-shear symplectic update

$$S_\tau = \begin{pmatrix} I & 0 \\ -\tau K_{\mathrm{ch}}/2 & I \end{pmatrix} \begin{pmatrix} I & \tau I \\ 0 & I \end{pmatrix} \begin{pmatrix} I & 0 \\ -\tau K_{\mathrm{ch}}/2 & I \end{pmatrix}. \tag{31}$$

For $\tau = 0.25$, the QCA is stable on the audited grid and has quasienergy exponent

$$z_\theta = 0.999784912034. \tag{32}$$

The effective frequency θ/τ has the same exponent and prefactor 0.099625201471. The sampled symplectic residual is

$$2.220446049250313 \times 10^{-16}, \tag{33}$$

with maximum eigenvalue-radius deviation 2.55×10^{-15}.

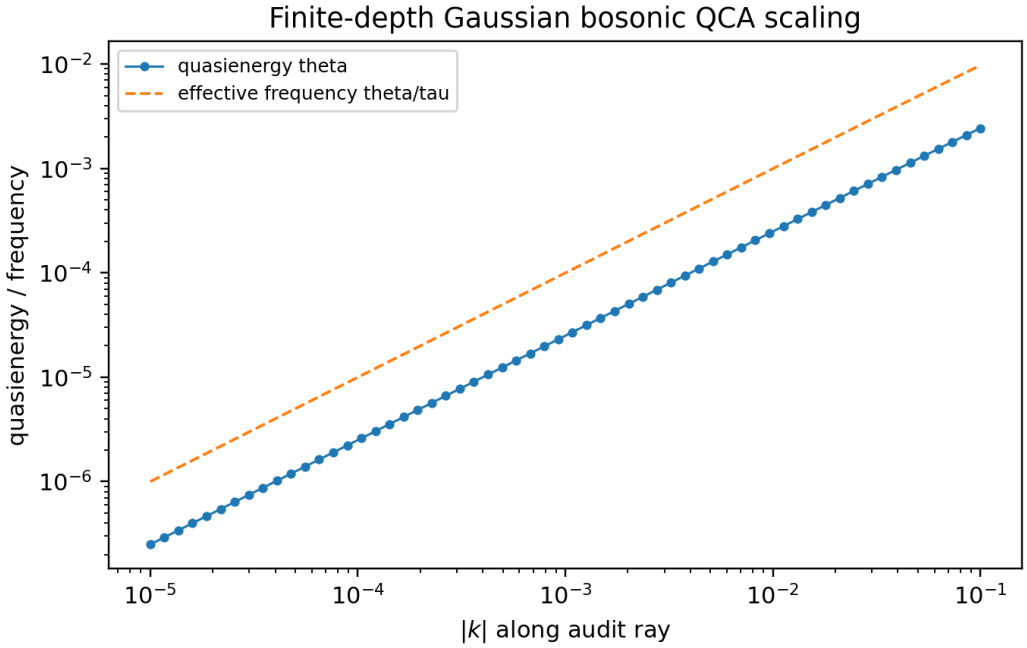

Figure 5: Quasienergy scaling of the finite-depth Gaussian bosonic QCA. The effective frequency θ/τ tracks the continuous oscillator frequency.

This QCA result is distinct from the earlier finite-prime Clifford QCA. The Clifford construction had the correct real tangent but finite-p arithmetic combs. The present object is a continuous-variable Gaussian symplectic automorphism, so it avoids the finite-field quasienergy comb at the price of using continuous oscillator variables.

8 Projected, auxiliary Ward, and local-source responses

Branch counting alone is not enough for a spin-2 response carrier. The next test is whether a conserved or TT-projected source sees the expected pole. For a source projected into the two-dimensional TT quotient, the static response of the chiral carrier fits

$$\chi_{\mathrm{TT}}(0,k) \sim |k|^{-1.999525292313}, \tag{34}$$

and the dynamical pole remains linear with exponent

$$z = 0.999761765187. \tag{35}$$

The small-k residue diagnostics agree:

$$\lambda_0 \chi(0,k) = 0.823598022519, \tag{36}$$

$$Z_{\mathrm{left}} = 0.823598006358, \tag{37}$$

$$(\lambda_0 - \omega^2)\chi(\omega, k)\big|_{\omega=0.5\omega_0} = 0.823598018479. \tag{38}$$

The TT Ward residuals are at numerical precision,

$$\|\mathrm{tr}\, P_{\mathrm{TT}}\|_\infty = 2.498 \times 10^{-16}, \qquad \|n \cdot P_{\mathrm{TT}}\|_\infty = 1.280 \times 10^{-18}. \tag{39}$$

Thus projected or externally conserved TT sources see the desired linear pole and static $1/k^2$ response.

The auxiliary local Ward-source audit improves this statement. Introduce a local symmetric stress variable S_{ij} subject to the local conservation law

$$d_i S_{ij} = 0. \tag{40}$$

Unlike exact local TT polynomial operators, a constrained stress variable with Eq. (40) has order-one TT content. After imposing the Ward constraint, the carrier sees the same static pole as a projected TT source,

$$\chi_{\mathrm{Ward}}(0, k) \sim |k|^{-2.000001654952}, \tag{41}$$

with branch exponent

$$z = 0.999999942266. \tag{42}$$

The local Ward geometry residuals are

$$\|DP_{\mathrm{div}}\|_\infty \le 1.224 \times 10^{-17}, \qquad \|DP_{\mathrm{TT}}\|_\infty \le 7.274 \times 10^{-17}, \tag{43}$$

$$\|\mathrm{tr}\, P_{\mathrm{TT}}\|_\infty \le 1.665 \times 10^{-16}. \tag{44}$$

A random constrained stress has mean TT weight fraction

$$0.663459, \tag{45}$$

consistent with the expected 2/3 dimension ratio inside the divergence-free subspace. This means the obstruction is not "a local stress can never have finite TT content." Rather, the stress must be an independent Ward-constrained variable or arise from a genuine matter Ward identity.

There is still a crucial local-source boundary. Strict derivative-built sources remain suppressed. In the local matter/Ward audit, a Beltrami-type local conserved source gave response scaling approximately

$$|k|^{1.999995874097}, \tag{46}$$

and an exact local TT Cotton source gave

$$|k|^{3.999995441147}. \tag{47}$$

Equivalently, the local polynomial enumeration found no nonzero divergence-free symmetric source below derivative degree $p = 2$, and no divergence-free traceless source below $p = 3$. Since the carrier contributes $1/k^2$, a source form factor k^p gives k^{2p-2}. Hence a finite-residue $1/k^2$ response requires either an independent conserved stress sector or a matter Ward identity, not a strictly local exact-TT operator built from the tensor variables alone.

9 Ward-completed dynamical matter coupling

The first dynamical matter test exposed a mass problem. If a dynamical local stress oscillator with finite static susceptibility is coupled nonderivatively as

$$H_{\mathrm{int}} = -g\, h_{ij} S_{ij}, \tag{48}$$

then integrating out the stress generates an effective stiffness shift

$$\lambda_{\rm eff}(k) = \lambda_{\rm carrier}(k) - g^2\chi_0. \tag{49}$$

Because $\lambda_{\rm carrier}(k) \sim k^2$, any fixed unprotected g is a relevant infrared perturbation. Derivative dressing protects the mass but destroys the long-range $1/k^2$ exchange by suppressing the source residue. Thus local conservation alone is not enough; the coupling and seagull must be tied by a stronger Ward or Goldstone symmetry.

The Ward-completed model supplies that mechanism at the effective CV/Gaussian level. For the two TT polarizations, introduce a local Ward-constrained stress coordinate S_a and complete the coupling as

$$H_m = \frac{\Omega^2}{2}\sum_a \left\|S_a - \alpha h_{{\rm wall},a}\right\|^2. \tag{50}$$

The term linear in $S_a h_{{\rm wall},a}$ gives the finite stress coupling, while the $h^2_{\rm wall}$ seagull is fixed by the same local positive square. It is not a tunable counterterm introduced after the fact.

At $k = 0$, let v_0 be the normalized lower-wall chiral null vector. The completed square is invariant under the diagonal shift

$$q_a \mapsto q_a + \epsilon v_0, \qquad S_a \mapsto S_a + \alpha v_0(0)\epsilon, \tag{51}$$

for $a = 1, 2$. Numerically,

$$\|D_0 v_0\| = 1.564 \times 10^{-17}, \qquad v_0(0)^2 = 0.823600000000, \tag{52}$$

and the two protected zero-vector residuals are

$$\|K_0 z_a\| = 1.122 \times 10^{-16}. \tag{53}$$

The first nonzero origin eigenvalue of the coupled model is

$$0.338173473027. \tag{54}$$

The coupled system has exactly two low positive TT branches at $|k| = 10^{-3}$. The fitted frequency exponents are

$$z_1 = 0.999606677871, \qquad z_2 = 0.999541049078. \tag{55}$$

The stress-source response sees the same long-range pole:

$$\chi_S(0,k) \sim |k|^{-1.999574909721}. \tag{56}$$

A random Ward-constrained stress source gives

$$\chi_{\rm random}(0,k) \sim |k|^{-1.999575423025}. \tag{57}$$

Near the first infrared sample, the lowest mode has left-wall weight

$$0.451634130284, \tag{58}$$

and stress weight

$$0.451634130284, \tag{59}$$

reflecting the hybridized diagonal Goldstone/stress mode.

The Ward stress geometry is clean at $|k| = 10^{-3}$:

$$\|DT_{\rm TT}\|_\infty = 2.800 \times 10^{-17}, \qquad \|\mathrm{tr}\, T_{\rm TT}\|_\infty = 5.551 \times 10^{-17}, \tag{60}$$

$$\|DS_{\rm scalar}\|_\infty = 2.262 \times 10^{-17}. \tag{61}$$

A random divergence-free stress has mean TT fraction

$$0.666936, \tag{62}$$

matching the expected 2/3.

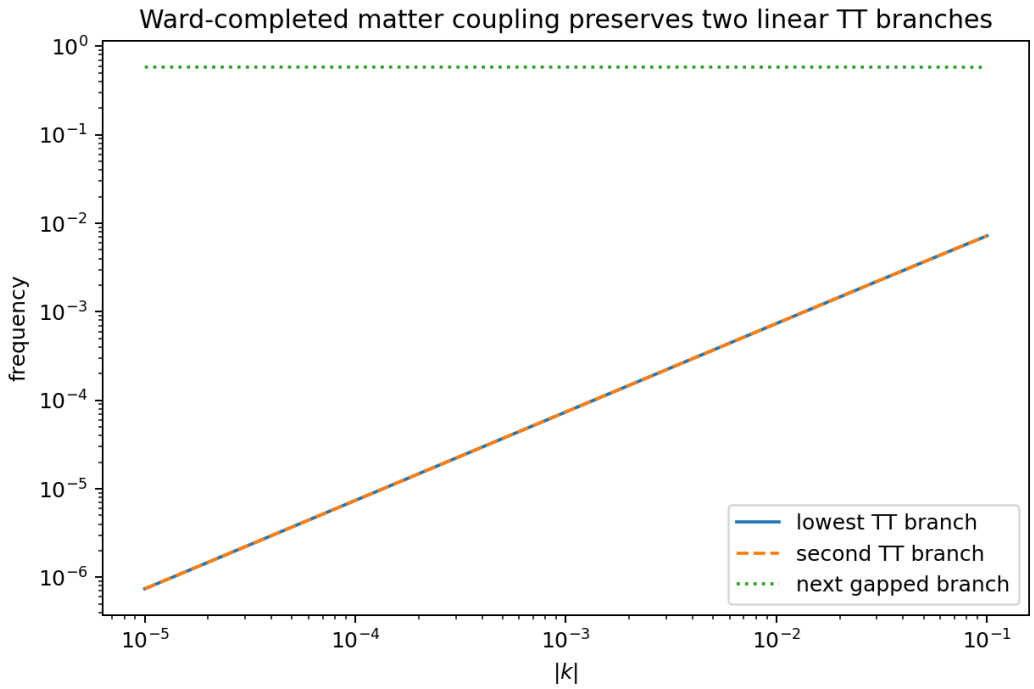

Figure 6: Infrared dispersion of the Ward-completed matter-coupled carrier. The two low positive TT branches remain linear after the stress coupling and symmetry-fixed seagull are included.

9.1 Seagull uniqueness and stability

The seagull coefficient is fixed by the square in Eq. (50). Detuning it below the Ward-completed value makes the origin mode unstable/tachyonic, while detuning it above opens a mass gap. The overtuned gap obeys

$$\Delta(\epsilon) \sim \epsilon^{0.493768802230}, \qquad R^2 = 0.999923387148, \tag{63}$$

consistent with the square-root law for a relevant mass perturbation. A no-cross control has minimum gap

$$0.581443136760. \tag{64}$$

Random local positive covariant-square perturbations that preserve the diagonal shift passed all tests:

$$64/64. \tag{65}$$

Their exponents lie in the ranges

$$0.999732450231 \le z \le 0.999866771840, \tag{66}$$

$$-1.999557074800 \le \alpha_\chi \le -1.999535470917, \tag{67}$$

and the minimum third origin eigenvalue among the protected samples is

$$1.365514 \times 10^{-2}. \tag{68}$$

Generic positive local wall terms that do not preserve the diagonal shift still gap the pole. The sampled generic gap range is

$$1.773063 \times 10^{-2} \le \Delta_{\text{generic}} \le 2.766510 \times 10^{-1}, \tag{69}$$

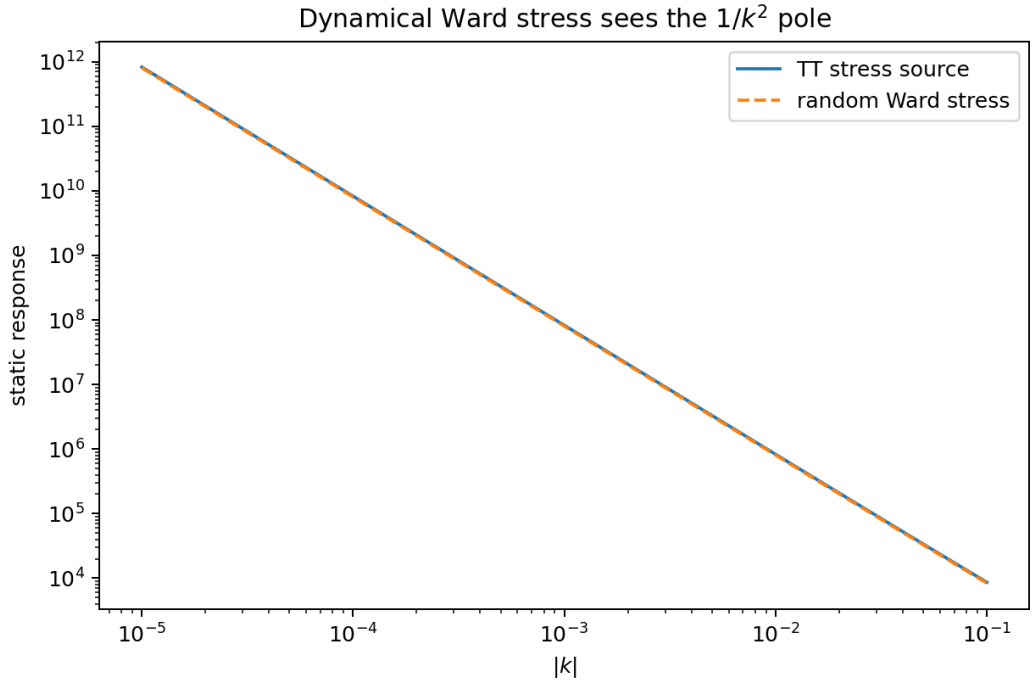

Figure 7: Ward-completed stress-source response. The local Ward stress sees the same $1/k^2$ infrared pole as the projected TT source, now with the seagull fixed by the covariant square.

with mean gap

$$1.041844 \times 10^{-1}. \tag{70}$$

This closes the immediate backreaction obstruction at the effective CV/Gaussian level. The local Ward stress has finite residue, the seagull is symmetry-fixed by the same square that supplies the stress coupling, and the massless pole is protected inside the diagonal-shift family. The remaining boundary is microscopic: the present matter sector is an effective local CV Ward sector, not yet a finite-d matter Hamiltonian or native QATNU phase.

10 Boundary-shift mass protection in the CV carrier

First-classness alone does not forbid a positive local mass term. The chiral CV carrier has a sharper protection mechanism: an exact lower-wall boundary-shift symmetry. The Ward-completed matter square in Sec. 9 is the dynamical-source version of this same mechanism: the stress variable shifts with the wall Goldstone so that the seagull and source coupling are symmetry-linked. At $k = 0$, the chiral factor has a null vector

$$v_0 \propto (1, r_0, r_0^2, \ldots, r_0^{W-1}), \tag{71}$$

with

$$D_0 v_0 = 0, \qquad K(0) v_0 = 0. \tag{72}$$

The corresponding shift generator is

$$\Pi_0 = \sum_s (v_0)_s p_s. \tag{73}$$

The numerical symmetry certificate gives

$$\|D_0 v_0\| = 1.563699 \times 10^{-17}, \qquad \|K(0) v_0\| = 1.589912 \times 10^{-17}, \tag{74}$$

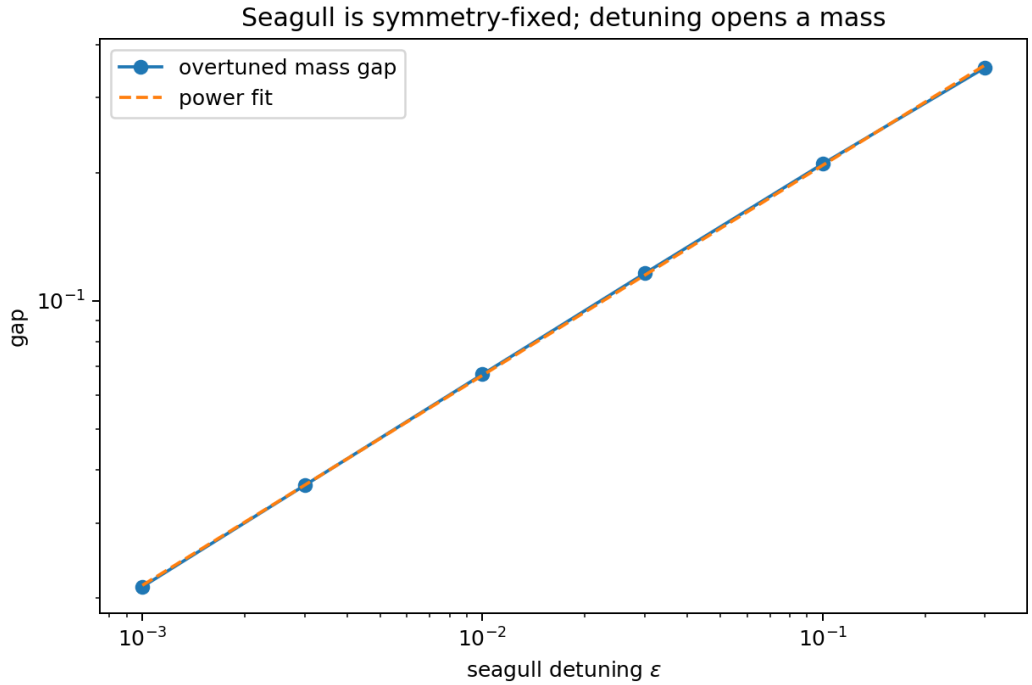

Figure 8: Seagull detuning audit. The Ward-completed value is the protected point. Undertuning is unstable, while overtuning opens a mass gap with the expected square-root scaling.

with second gap

$$\Delta_2(0) = 0.581548368134. \tag{75}$$

The protected perturbation ensemble used local positive terms constrained to preserve this boundary shift,

$$K(k) = K_{\mathrm{ch}}(k) + \alpha D_0^T C^T C D_0 + \beta m_W(k) B^T B + \gamma \left\| n(k) \right\|^2 E^T E. \tag{76}$$

All 64/64 tested samples retained one scalar soft branch, $z \simeq 1$, static response exponent near -2, and $K(0)v_0 = 0$. The frequency exponents ranged from

$$0.999937284 \leq z \leq 0.999998718, \tag{77}$$

and the static response exponents from

$$-1.999997372 \leq \alpha_\chi \leq -1.999824064, \tag{78}$$

with minimum infrared residue

$$Z_{\min} = 0.823572697716. \tag{79}$$

By contrast, generic local positive first-class copy-space terms need not preserve the boundary shift. Their origin gaps ranged from

$$5.033427 \times 10^{-5} \quad \text{to} \quad 7.058888 \times 10^{-2}, \tag{80}$$

and their deep-infrared response collapsed toward massive scaling. Thus the carrier is not merely fine-tuned inside the CV chiral family, but the protection is a continuous/noncompact boundary-shift symmetry. Promoting it to an exact fixed-local-dimension phase still requires a finite-spin, rotor, topological-order, or matter-Ward implementation of the same symmetry logic.

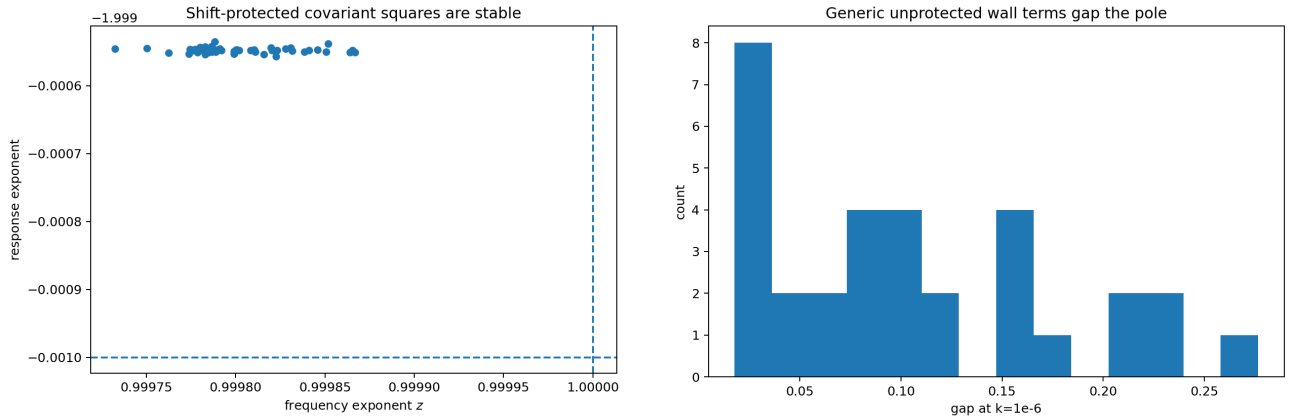

Figure 9: Left: protected covariant-square perturbations preserve the linear pole and $1/k^2$ response. Right: generic wall terms that do not preserve the diagonal shift open a mass gap.

11 Controlled finite-local-dimension truncation

The next question is whether the continuous oscillator lift hides an infrared local-variance catastrophe. In three spatial dimensions it does not. After removing the single homogeneous zero oscillator, the local covariance converges with box size in the audit.

At the largest audited box, $L = 24$ with synthetic width $W = 16$,

$$\max_s \langle q_s^2 \rangle = 0.397764924326, \tag{81}$$

$$\max_s \langle p_s^2 \rangle = 1.219767160624, \tag{82}$$

$$\max_s \bar{n}_s = 0.167701370515. \tag{83}$$

The $L \to \infty$ extrapolation gives

$$\max_s \langle q_s^2 \rangle_\infty \simeq 0.400151411669, \qquad \max_s \bar{n}_s \simeq 0.170917403179. \tag{84}$$

In the optimized one-site oscillator basis, the thermal ratio is

$$\eta = \frac{\bar{n}}{1+\bar{n}} = 0.145968795677, \tag{85}$$

so a Fock/qudit cutoff at local dimension d has tail

$$P(n \geq d) = \eta^d. \tag{86}$$

The required onsite dimensions are small for local observables:

tail target	10^{-4}	10^{-6}	10^{-8}	10^{-10}
required d	5	8	10	12

(87)

At $d = 8$ the tail is 2.061010×10^{-7}, and at $d = 10$ it is 4.391372×10^{-9}.

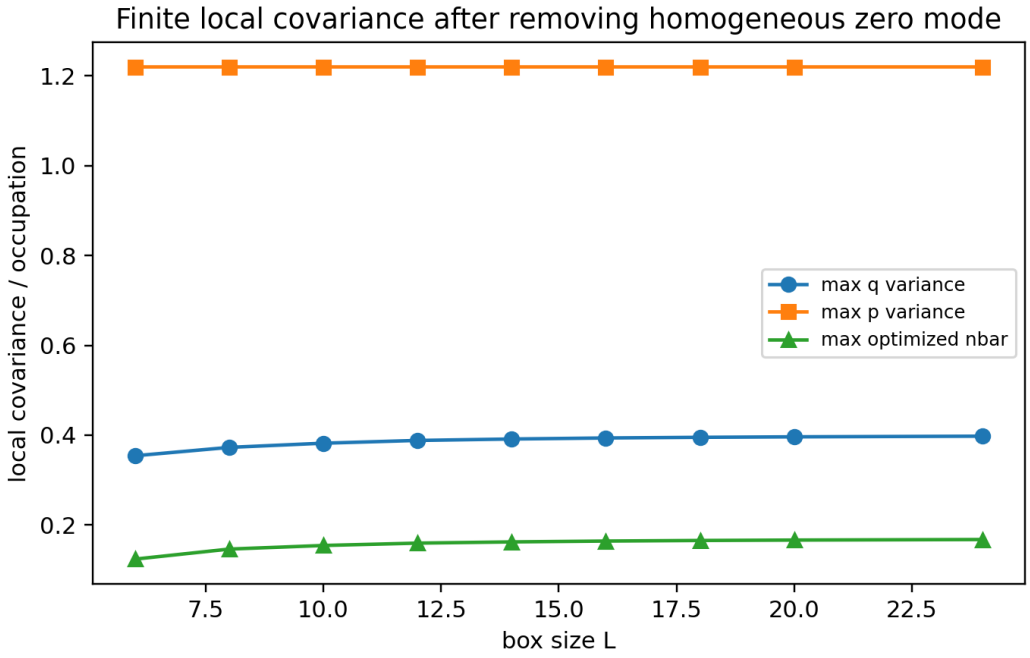

Figure 10: Local covariance and optimized local occupation versus box size after removing the homogeneous zero oscillator. The quantities approach finite values in the audited three-dimensional model.

11.1 Finite-resource approximation laws

The approximation-law audit packages the local truncation, guard crossover, global no-leakage, and finite-range Ward-source errors into explicit scaling laws. With

$$\eta = 0.145968795676762, \tag{88}$$

the local tail and top-level CCR/Ward proxy are

$$P_{\mathrm{tail}}(d) = \eta^d, \qquad \delta_{\mathrm{CCR}}(d) = d(1-\eta)\eta^{d-1}. \tag{89}$$

The positive onsite guard gap is fit by

$$\Delta_{\mathrm{guard}}(d,\lambda) \simeq 2.37213\sqrt{\lambda\,\delta_{\mathrm{CCR}}(d)}, \qquad R^2 = 0.999999976, \tag{90}$$

and the associated clean finite-size window is

$$L_\star(d,\lambda) = \frac{2\pi c}{\Delta_{\mathrm{guard}}(d,\lambda)}, \qquad c = 0.099609932405. \tag{91}$$

For $\lambda = 1$, selected values are

d	8	10	12	16
P_{tail}	2.0610×10^{-7}	4.3914×10^{-9}	9.3566×10^{-11}	4.2478×10^{-14}
δ_{CCR}	9.6468×10^{-6}	2.5693×10^{-7}	6.5692×10^{-9}	3.9764×10^{-12}
Δ_{guard}	7.3677×10^{-3}	1.2024×10^{-3}	1.9226×10^{-4}	4.7303×10^{-6}
$L_\star$	84.95	520.52	3255.27	1.323×10^{5}

(92)

This is the operational meaning of the finite-qudit result: fixed d can provide an enormous clean window for local IR observables, but a positive guard is still a finite-size approximation rather than a fixed-d thermodynamic protection mechanism.

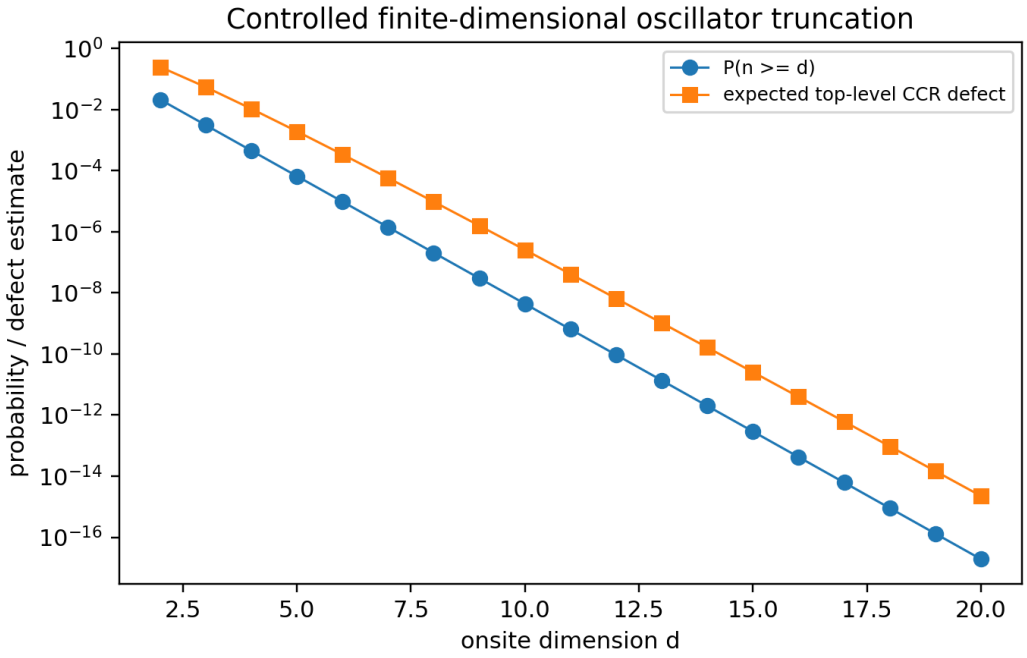

Figure 11: Local Fock/qudit tail and expected top-level CCR defect versus onsite dimension. The finite-dimensional regularization is controlled for local low-energy observables.

For a global exact no-leakage demand across WL^3 local oscillators,

$$\mathbb{E}[N_{\text{tail}}] = WL^3\eta^d, \tag{93}$$

so d must grow logarithmically with L. With $W = 16$, keeping $\mathbb{E}[N_{\text{tail}}] < 10^{-6}$ requires $d = 16$ at $L = 64$, $d = 20$ at $L = 1024$, and $d = 31$ at $L = 10^6$.

The local-source approximation law is harsher. A finite-range surrogate for the nonlocal TT source compiler modeled by a Yukawa mass $m = 1/R$ has lowest-mode Ward residual

$$\epsilon_{\text{Ward}}(k_{\min}, R) = \frac{m^2}{k_{\min}^2 + m^2}, \qquad k_{\min} = \frac{2\pi}{L}. \tag{94}$$

Maintaining fixed Ward accuracy at the deepest box mode requires $R \propto L$. This restates the source-coupling obstruction quantitatively: exact local low-derivative TT coupling is not obtained by a finite-range compiler at fixed range.

11.2 Large-spin and finite-grid alternatives

The large-spin Holstein-Primakoff encoding

$$q_J = \frac{S_x}{\sqrt{J}}, \qquad p_J = \frac{S_y}{\sqrt{J}} \tag{95}$$

has

$$[q_J, p_J] = i\frac{S_z}{J} = i\left(1 - \frac{N}{J}\right). \tag{96}$$

At $J = 64$, with local dimension 129, the expectation-level CCR defect is 2.670584×10^{-3}. Strict operator-norm control on the tail-10^{-6} subspace is much more expensive, about 1.09375×10^{-1} at

$J = 64$. Thus the large-spin route is a valid code-sector interpretation, but direct Fock/qudit truncation is more efficient for this audited architecture.

A finite-grid/DVR oscillator can approximate individual oscillator gaps accurately at fixed target frequency, but it does not remove the basic finite-matrix trace obstruction discussed below. It is therefore a simulator regularization, not an exact local canonical algebra.

12 Why a simple protected fixed-d phase is still missing

The controlled finite-dimensional truncation does not by itself prove an exact fixed-local-dimension phase. Two obstructions remain.

12.1 Trace obstruction for exact finite-dimensional CCR

Let $A = PQP$ and $B = P\Pi P$ be finite matrices acting on a nonzero local code space. Then

$$\mathrm{tr}[A, B] = 0. \tag{97}$$

Therefore $[A, B] = iI$ cannot hold on that finite-dimensional code space. The normalized Frobenius residual lower bound is at least one for every nonzero code dimension. Exact first-class canonical brackets cannot be obtained from a finite-dimensional local code by projection alone.

This is not a problem for local low-energy simulation, where top-level population controls the defect. It is a problem for claiming an exact finite-d phase with exact onsite canonical algebra.

12.2 Onsite positive guard is relevant

A natural protection attempt is the positive onsite guard

$$V_{\mathrm{guard}} = \lambda \sum_x |d-1\rangle_x \langle d-1|_x. \tag{98}$$

The audit shows that this guard has a nonzero quadratic component in the local Gaussian vacuum and therefore opens a mass gap in the soft branch unless a counterterm is tuned. At $\lambda = 1$ the gaps are listed in Table 4.

Table 4: Onsite guard-induced gap estimates. The crossover scale is $L \sim 2\pi c/gap$.

d	Guard-induced gap	Crossover L	Expected CCR defect
5	1.044439×10^{-1}	5.99	1.938581×10^{-3}
8	7.360448×10^{-3}	85.0	9.646814×10^{-6}
10	1.190861×10^{-3}	525.6	2.569295×10^{-7}
12	1.884708×10^{-4}	3.32×10^{3}	6.569242×10^{-9}
16	4.530247×10^{-6}	1.38×10^{5}	3.976437×10^{-12}

One can fine-tune a quadratic counterterm to restore the cone, but then masslessness is tuned rather than protected by the positive guard. A successful fixed-d phase would need a many-body or symmetry protection mechanism that forbids the mass term, rather than an onsite cutoff penalty.

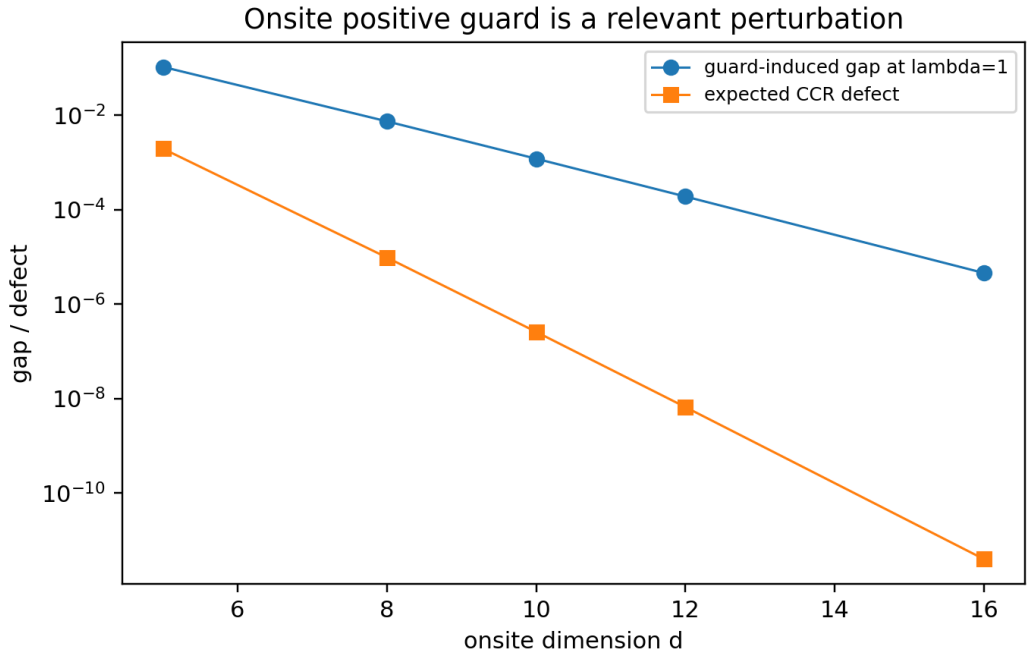

Figure 12: A positive top-level onsite guard opens a mass gap at fixed d and fixed coupling. Increasing d makes the clean finite-size window very long, but does not produce an exact fixed-d thermodynamic phase.

12.3 Global no-leakage versus local control

For local observables, fixed d controls the reduced local tail. A stronger demand, exact global no-leakage over all WL^3 oscillators, is different. The expected number of tail sites scales as

$$\mathbb{E}[N_{\text{tail}}] = WL^3\eta^d. \tag{99}$$

Therefore d must grow logarithmically with L to keep the global no-leakage probability fixed. The audit finds, for example,

L	d for $\mathbb{E}[N_{\text{tail}}] < 10^{-3}$	d for $\mathbb{E}[N_{\text{tail}}] < 10^{-6}$
64	12	16
1024	16	20
10^6	27	31

(100)

13 Compact-rotor and finite-spin Ward-square route

The finite-dimensional route should not try to make finite matrices satisfy $[q, p] = iI$. Instead, the finite-spin audit rewrites the Ward-completed square as a compact diagonal $U(1)$ target. The massless carrier is then a Goldstone mode of a symmetry, not an onsite canonical algebra.

In the localized CV profile used above, the null vector at $k = 0$ is $v_0 \propto (1, r_0, r_0^2, \ldots)$ with $r_0 = 0.42$. A literal compact lock $\theta_{s+1} - r_0\theta_s$ would require rational integer charges, e.g. $21\theta_s - 50\theta_{s+1}$ for $r_0 = 21/50$, producing a large microscopic charge hierarchy. The finite-spin audit therefore compared rational profiles with the simple compact profile

$$r_0 = 1, \qquad D_0\theta_s = \theta_{s+1} - \theta_s. \tag{101}$$

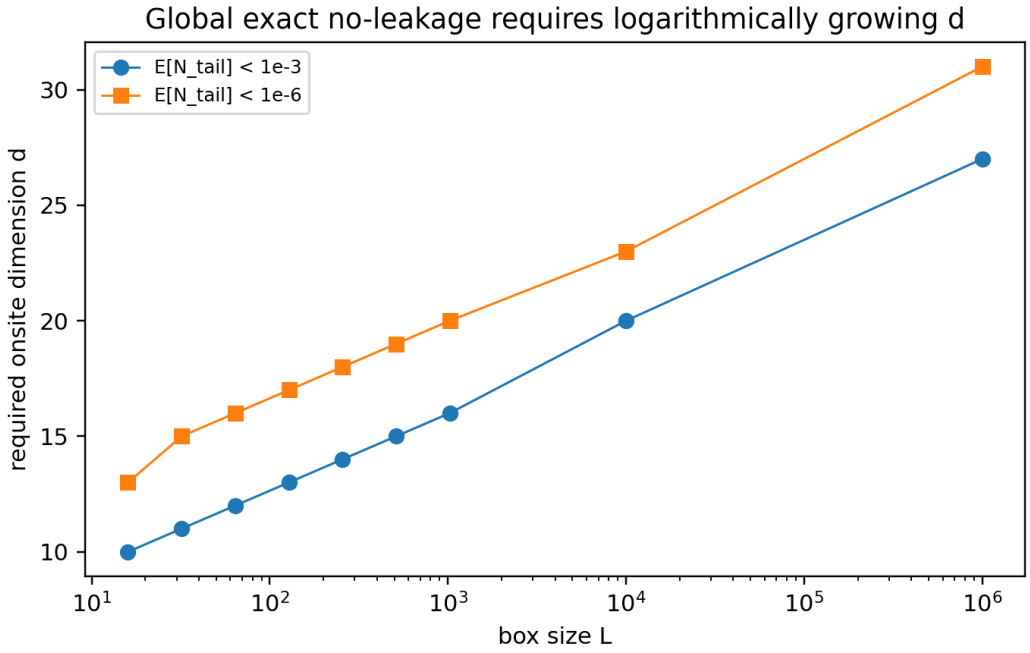

Figure 13: Fixed onsite dimension controls local reduced tails, but global exact no-leakage requires logarithmically growing d as volume increases.

The simple profile has weaker wall localization but no charge hierarchy. It keeps the desired spin-2 response at fixed synthetic width:

$$N_{\mathrm{low}} = 2, \qquad z = 0.999766925, \qquad \chi_S(0,k) \sim k^{-1.999568522}. \tag{102}$$

The finite residue is smaller but nonzero,

$$Z_S = \frac{1}{17} = 0.0588235, \tag{103}$$

with second scalar gap 0.184536719 and known-doubler gap 0.939317691 in the audited compact target.

Table 5: Compact profile tradeoff in the Ward-square rotor audit. Localized profiles increase residue and the second gap but require larger integer charge locks; the simple $r_0 = 1$ profile avoids the hierarchy.

Variant	r_0	z	χ exponent	residue	second gap
legacy	21/50	0.999889499	−1.999528800	0.451634	0.593197
localized	1/2	0.999867091	−1.999531467	0.428571	0.517969
moderate	2/3	0.999815061	−1.999536570	0.357143	0.367524
simple	1	0.999766925	−1.999568522	0.0588235	0.184537

For the simple $r_0 = 1$ target, shift-preserving positive perturbations passed 64/64 samples. They retained

$$z \in [0.999742637, 0.999803541], \qquad \alpha_\chi \in [-1.999579081, -1.999559149], \tag{104}$$

where $\chi \sim k^{\alpha_\chi}$. Generic shift-breaking wall/stress terms opened gaps in the range

$$\Delta \in [2.27516 \times 10^{-4}, 5.79308 \times 10^{-2}]. \tag{105}$$

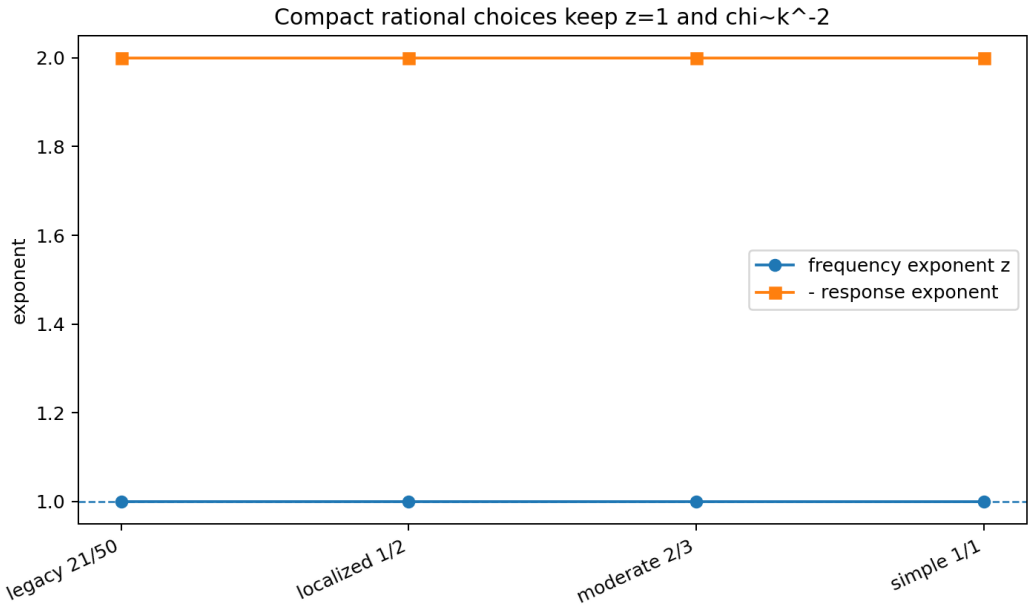

Figure 14: Compact profile exponent audit. All tested profiles retain $z \simeq 1$ and $\chi_S(0,k) \sim k^{-2}$ at the spin-wave level.

This repeats the CV lesson in compact language: the diagonal Ward $U(1)$ is essential.

A large-spin realization around an ordered direction has

$$q_J \sim \frac{S^y}{\sqrt{J}}, \qquad p_J \sim \frac{S^z}{\sqrt{J}}, \qquad [q_J, p_J] = i\frac{S^x}{J} \simeq i\left(1 - \frac{N}{J}\right). \tag{106}$$

Using the audited local occupation for the compact target, the Holstein-Primakoff expectation-level defect scales as $\bar{n}/J$. The estimates are:

J	16	32	64	128
$2J+1$	33	65	129	257
HP defect	5.959×10^{-3}	2.980×10^{-3}	1.490×10^{-3}	7.449×10^{-4}

(107)

This is qualitatively different from the onsite cutoff guard. The candidate finite-dimensional phase would be protected by an ordered compact symmetry sector; the finite onsite Hilbert space approximates the Goldstone variables inside that sector rather than satisfying exact CCR as a local matrix identity.

This section is still a spin-wave and code-sector result, not a nonperturbative phase proof. The remaining finite-spin obligations are to show that the ordered compact phase exists with controlled vortices/phase slips, that lattice anisotropies do not generate a mass, that the Ward stress Gauss law is implemented microscopically, and that no extra Goldstone branches or mirror cones reappear.

14 Local Ward-stress Gauss law and covariant seagull localization

The Ward-completed square changes the role of the matter source. A local symmetric stress coordinate S_{ij} subject to the microscopic Gauss law

$$G_j(x) = \sum_i \left[S_{ij}(x) - S_{ij}(x - \hat{e}_i)\right] = 0 \tag{108}$$

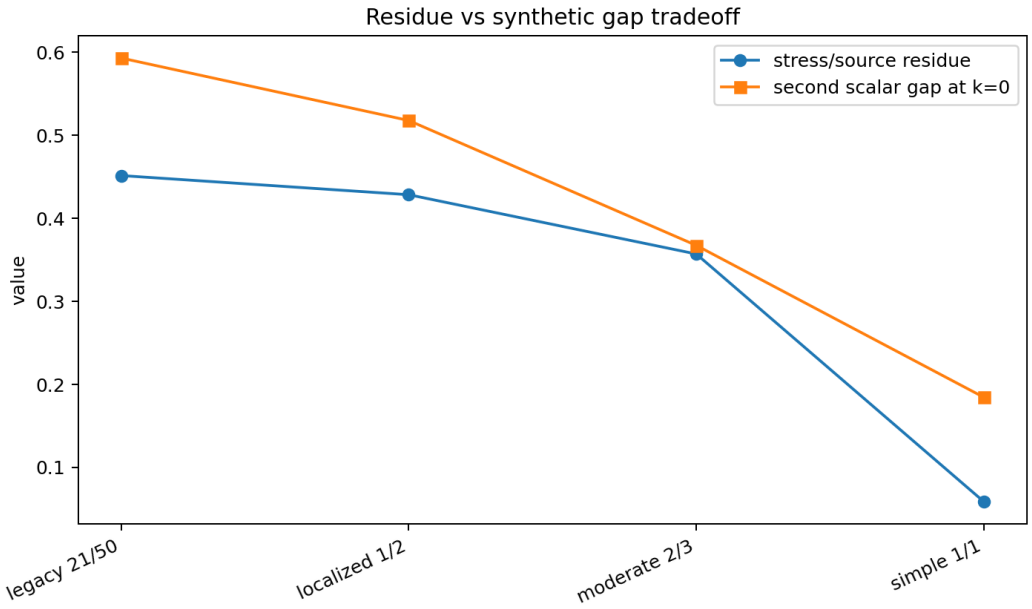

Figure 15: Residue/gap versus compact charge cost. The simple $r_0 = 1$ model sacrifices localization but avoids large microscopic integer charges, making it the preferred finite-spin target.

has order-one TT content without being a derivative-built Beltrami or Cotton source. At nonzero momentum, adding the local trace condition makes the source exactly TT:

$$d_i S_{ij} = 0, \qquad \operatorname{tr} S = 0. \tag{109}$$

Finite-lattice rank checks give

$$\operatorname{rank}(\nabla \cdot S) = 3(V-1), \qquad \operatorname{rank}(\nabla \cdot S, \operatorname{tr} S) = 4V - 3, \tag{110}$$

so the trace-free Ward-stress sector has $2V + 3$ coordinate degrees of freedom: two local TT stress polarizations at each nonzero momentum plus global uniform trace-free modes. Random divergence-free stresses have mean TT fraction $0.664049 \simeq 2/3$, while divergence-free traceless stresses have TT fraction 1.

The first simple attempt at the seagull failed. The source cross-term $S_{ij}A_{ij}$ is first class when S is constrained, but the required order-one A^2 seagull is not. The normalizer residuals for local candidates were order one:

candidate	max normalizer residual
$A_{ij}A_{ij}$	9.297457×10^{-1}
local trace-free square	8.567429×10^{-1}
divergence-free projected square	5.229963×10^{-1}
exact TT-projected square	5.034238×10^{-16}
Cotton-order TT character	2.259854×10^{-17}

(111)

Thus the direct order-one seagull is the exact TT projector, and the exact projector has an algebraic real-space tail. The local Cotton alternative is first class but derivative-suppressed and cannot supply the desired order-one stress coupling.

The escape is to enlarge the local field space rather than to approximate the projector. Define the covariant relative tensor

$$R_{ij} = S_{ij} - \alpha A_{ij} \tag{112}$$

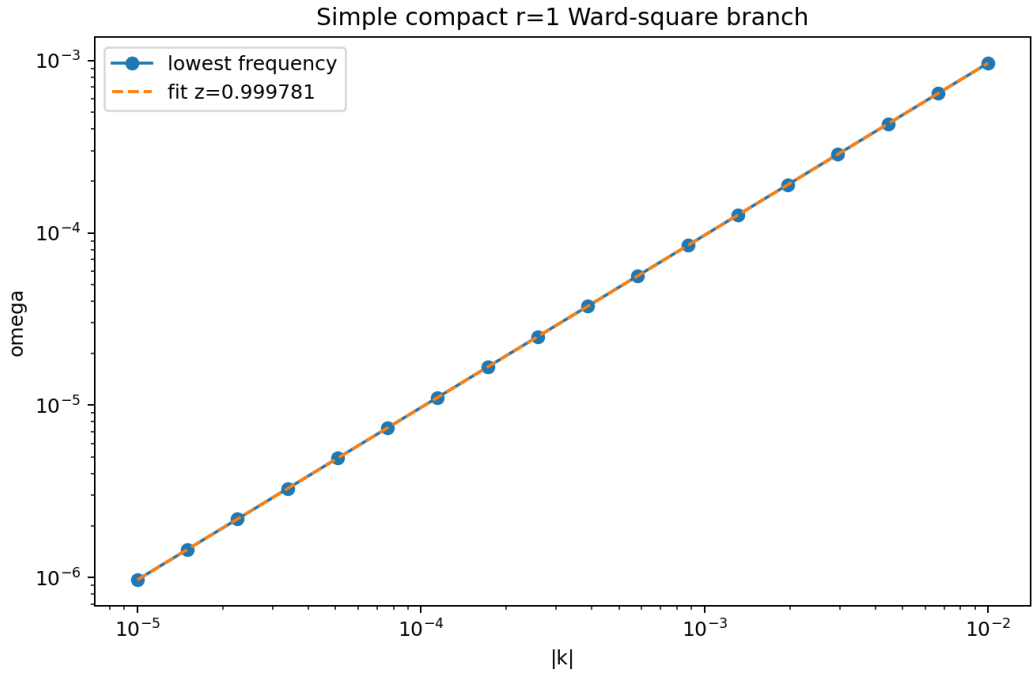

Figure 16: Simple $r_0 = 1$ compact-rotor frequency scaling.

and impose local constraints directly on R:

$$\nabla_i R_{ij} = 0, \qquad \operatorname{tr} R = 0. \tag{113}$$

Then the local square

$$H_{\text{square}} = \frac{\Omega^2}{2}\|R\|^2 \tag{114}$$

is invariant under the combined gauge/trace shift

$$\delta A = g, \qquad \delta S = \alpha g, \tag{115}$$

because R itself is invariant. Eliminating the local constraints regenerates the TT projector, but this nonlocality is now the ordinary nonlocality of solving a Gauss law, not a microscopic long-range kernel.

The constraint nullspace matches the analytic TT projector with residual 5.413×10^{-12}, the divergence and trace residuals on the constrained nullspace are 2.584×10^{-16} and 6.384×10^{-16}, and the expanded square has exact combined-shift null residual. For the compact $r_0 = 1$ target the same audit gives

$$z = 0.999999803, \qquad \chi_S(0,k) \sim k^{-1.999989379}, \qquad Z_S = \frac{1}{17}, \tag{116}$$

with second gap 0.184536719, low TT branch count 2 at $|k| = 10^{-3}$, and 64/64 shift-preserving perturbations passing.

15 Full compact tensor/matter Ward-square target

The full assembled compact target uses a matter stress tensor and a synthetic chain of tensor variables,

$$S_{ij}, \qquad A_{ij}(s), \qquad s = 0, \ldots, W-1, \tag{117}$$

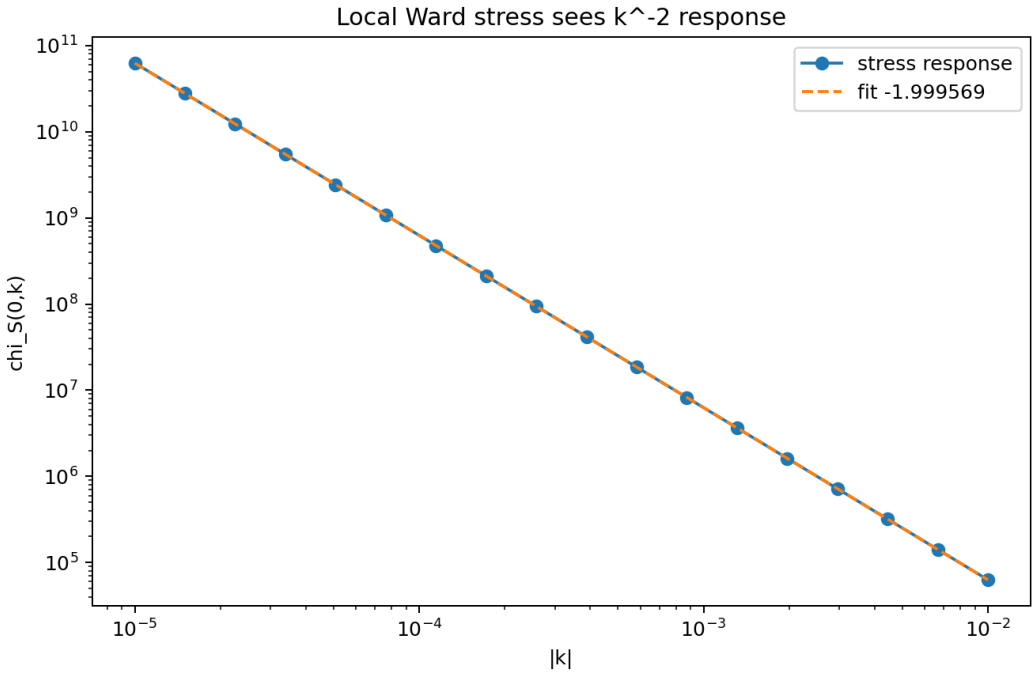

Figure 17: Simple $r_0 = 1$ compact-rotor source response scaling.

with the relative tensor

$$R_{ij} = S_{ij} - A_{ij}(0). \tag{118}$$

The local constraints are

$$\nabla_i A_{ij}(s) = 0, \quad \operatorname{tr} A(s) = 0, \quad \nabla_i R_{ij} = 0, \quad \operatorname{tr} R = 0. \tag{119}$$

The harmonic compact path target is

$$K(k) = L_{\text{path}} \otimes I_6 + |d(k)|^2 I. \tag{120}$$

For $W = 16$, the full symbol has 102 tensor coordinates, 68 local constraint rows at nonzero momentum, and constrained dimension

$$34 = 2W + 2. \tag{121}$$

The finite-lattice rank checks match

$$\operatorname{rank} C = (W+1)(4V-3), \qquad \dim\ker C = (W+1)(2V+3) \tag{122}$$

for the tested boxes $(L, W) = (2, 2), (2, 4), (3, 2)$.

The full constrained harmonic quotient has exactly two low branches:

$$z_1 = 0.999999525, \qquad z_2 = 0.999999518, \tag{123}$$

and stress response exponents

$$-1.997024224, \qquad -1.997024228. \tag{124}$$

The third branch remains gapped, $\Delta_3 \simeq 0.184536746$. If only the relative R constraint is imposed, the low tensor branch count is 6 rather than 2, so the full tensor quotient is doing real work.

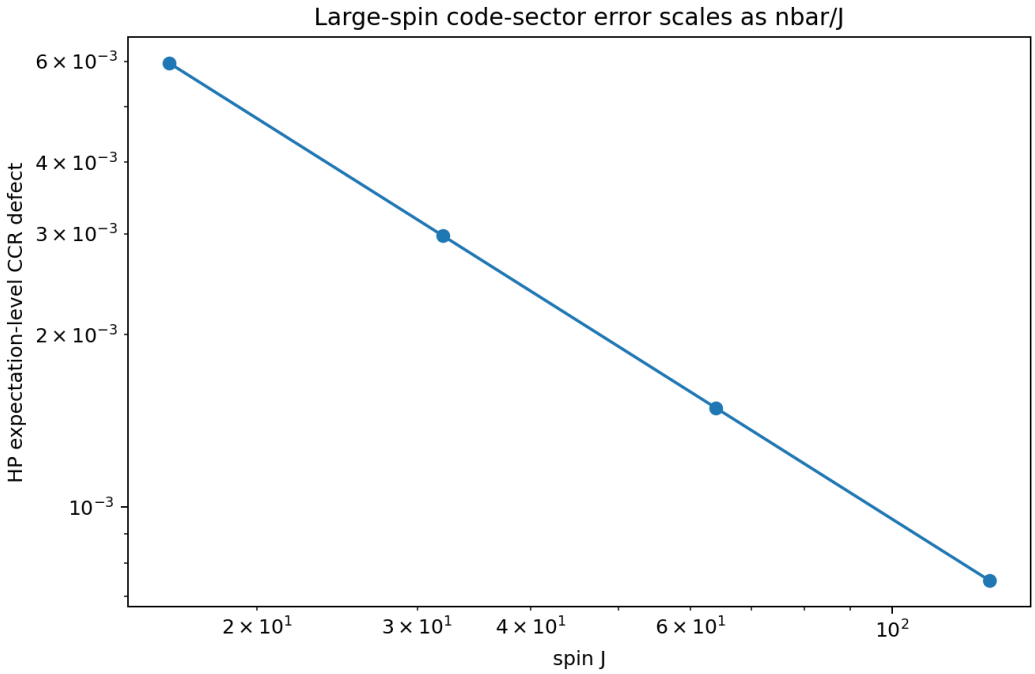

Figure 18: Large-spin Holstein-Primakoff defect estimate for the compact Ward-square target.

A soft compact Metropolis pilot of the unfactored variables at $L = 3$, $W = 2$, $\beta = 1.2$, path stiffness 8, and charge stiffness 20 gives mean magnetization 0.985901, minimum component magnetization 0.970789, path-lock RMS 0.187089, constraint RMS 0.191536, and zero detected defects. Larger soft compact screens remain ordered: at $L = 5$, $W = 4$, one finds $|m| = 0.982363$, path RMS 0.203788, divergence RMS 0.202331, trace RMS 0.188163, and zero charge defects.

16 Hard constraints, finite spin, and compact phase screens

The hard-constrained spectral audit imposes the divergence and trace constraints by exact null-space elimination. It does not insert a microscopic TT projector and it does not use soft penalties. The hard-constrained quotient gives one scalar soft branch, hence two TT branches after tensoring with the two TT labels:

$$N_{\mathrm{low}}^{\mathrm{TT}} = 2, \qquad z = 0.999493439, \qquad \chi_S(0,k) \sim k^{-1.998965499}. \tag{125}$$

The IR residue is

$$\langle \lambda_0(k)\chi_S(0,k)\rangle_{\mathrm{IR}} = 0.058823546, \qquad \frac{1}{W+1} = \frac{1}{17} = 0.058823529. \tag{126}$$

The next branch gap at the smallest audited k is 0.184536719. A 13^3 Brillouin-zone scan checked 2196 nonzero momentum points and found no extra zero below 10^{-8}, with minimum next scalar gap 0.191816426 and known-doubler frequency 0.639905158.

The hard-constrained compact spin screen then samples directly in hard quotient variables. The

ordered sector stays stable in the tested sizes:

L	W	$\lvert m\rvert$	Υ_x	f_{vortex}	path RMS
4	4	0.927092	1.119224	0	0.269976
6	4	0.956566	1.119581	0	0.269236
8	4	0.958911	1.119222	0	0.268702
4	8	0.941753	1.125595	0	0.263631

(127)

Thus the hard quotient screen has finite phase stiffness, strong ordering, suppressed compact defects, and stable synthetic locking in the audited range.

Finite-spin saturation is also controlled. After removing the global diagonal zero, the ordered-sector local spin-wave density remains bounded. At $L = 24$, $W = 16$ the audit finds

$$\max_s \langle q_s^2 \rangle = 0.539157941, \qquad \max_s \langle p_s^2 \rangle = 1.388823655, \qquad \bar{n}_{\max} = 0.020820302, \tag{128}$$

with extrapolated

$$\bar{n}_{\max,\infty} \simeq 0.020757175. \tag{129}$$

Hence the Holstein-Primakoff defect scales as $\bar{n}/J$ without growing with L in the ordered-sector estimate. Representative finite-spin bounds are

J	$2J+1$	δ_{HP}	pole fraction lower bound
8	17	2.595×10^{-3}	0.989621
16	33	1.297×10^{-3}	0.994811
32	65	6.487×10^{-4}	0.997405
64	129	3.243×10^{-4}	0.998703

(130)

This removes finite-spin saturation as the leading obstruction in the ordered sector.

17 Microscopic finite-spin quantum box

The latest check is an explicit finite-dimensional quantum box, rather than a harmonic symbol or classical compact screen. The model is a reduced one-polarization hard-quotient compact Ward-square box: an $L = 3$ spatial ring times a minimal matter/tensor chain, with compact rotors truncated to $|n| \le J$. Equivalently this is a finite-spin ladder with a hard flux ceiling. The Hamiltonian has the form

$$H = \frac{1}{2} \sum_x \hat{n}_x^2 + \sum_{\langle xy \rangle} \big(1 - \cos(\theta_x - \theta_y)\big), \tag{131}$$

with spatial ring bonds on the tensor nodes and path locks including the matter node, realizing the covariant square at $\alpha = \Omega = 1$. The largest reported exact sparse diagonalization uses $1,953,125$ states.

The box separates the compact ordered-sector Anderson tower from the dispersing magnon branch. The charge tower obeys the expected Q^2 law and converges toward a finite renormalized moment of inertia: for $Q = 1$,

$$E_{Q=1} = 0.161944, 0.096723, 0.091255, 0.0911 \tag{132}$$

for $J = 1, 2, 3, 4$. The harmonic value is 0.0833, so the finite compact box has a roughly 9% anharmonic shift.

The nonzero-momentum magnon branch converges rapidly. At $k = 2\pi/3$,

$$\omega(k) = 0.80484, 0.74001, 0.73890, 0.73888 \tag{133}$$

for $J = 1, 2, 3, 4$. The bare harmonic reference is 0.83500; the compact interacting branch is stable and softened by about 11.5%.

The matter operator also retains a finite single-pole fraction. For the local probe $e^{i\theta_0}$, the pole fraction is

$$0.4850, 0.4351, 0.4308, 0.4306 \tag{134}$$

for $J = 1, 2, 3, 4$, close to the box's harmonic Debye-Waller prediction 0.416. The remaining weight is the expected multi-magnon continuum. In a larger $L = 3 \times N = 3$ box, the $k = 0$ matter weight sits predominantly on the tower state itself, with reported fraction about 83%.

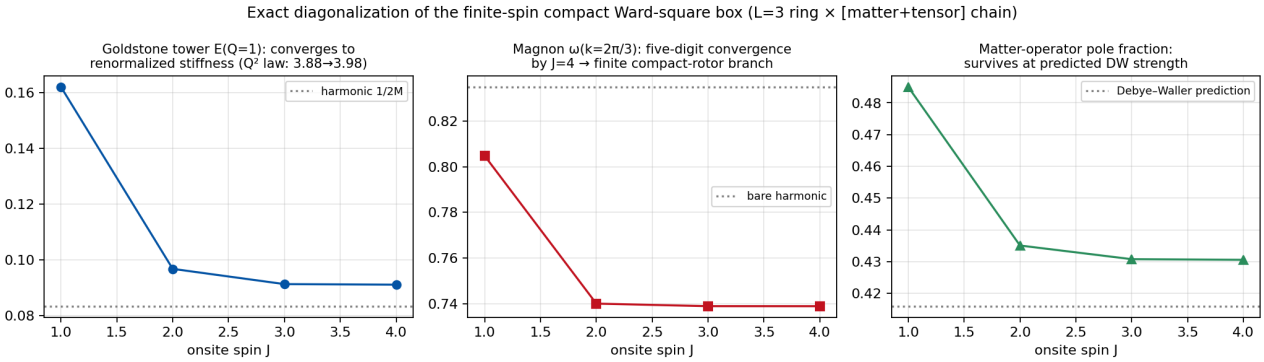

Figure 19: Finite-spin compact Ward-square quantum box. Left: the Anderson tower converges toward a finite renormalized stiffness. Middle: the $k = 2\pi/3$ magnon frequency converges by $J = 4$. Right: the matter-operator pole fraction remains finite and approaches the Debye-Waller estimate for the same box.

A dispersion box at $L = 6$, $N = 2$, $J = 1$ gives

$$\omega(\pi/3) = 0.587, \qquad \omega(\pi) = 0.772, \tag{135}$$

compared with harmonic references 0.618 and 0.874. This is a monotone dispersing branch with uniform anharmonic softening. The low states in the audited charge and momentum sectors are accounted for as tower plus magnons, with no extra soft states detected in the box.

17.1 Tower-filtered dynamic structure factor

The finite-spin box data become sharper when expressed as a tower-filtered structure factor. The Anderson tower is the $Q = 1, k = 0$ rotor line. At finite momentum $k = 2\pi/3$, the Fourier source vector has no tower pole; the dominant line is the magnon/source pole. The audited dynamic structure factor is

$$S_{SS}(k, \omega) = \sum_n |\langle n|S(k)|0\rangle|^2 \delta(\omega - E_n + E_0), \tag{136}$$

with $S(k)$ represented in the compact box by the matter rotor raising operator with spatial Fourier phase.

For the $L = 3, N = 2$ box, the tower-filtered diagnostics are

J	$E(Q = 1)$	$\omega(2\pi/3)$	pole fraction	captured window
1	0.161944	0.80484	0.4850	0.998
2	0.096723	0.74001	0.4351	0.947
3	0.091255	0.73890	0.4308	0.946
4	0.091100	0.73888	0.4306	0.946

(137)

The harmonic references are $E(Q=1) = 1/12$, $\omega(2\pi/3) = 0.83500$, and Debye-Waller pole fraction 0.416. Thus the $J = 4$ tower has a finite renormalized moment of inertia, while the finite-k pole is softened by 11.5% and keeps a pole fraction within 3.5% of the box Debye-Waller estimate.

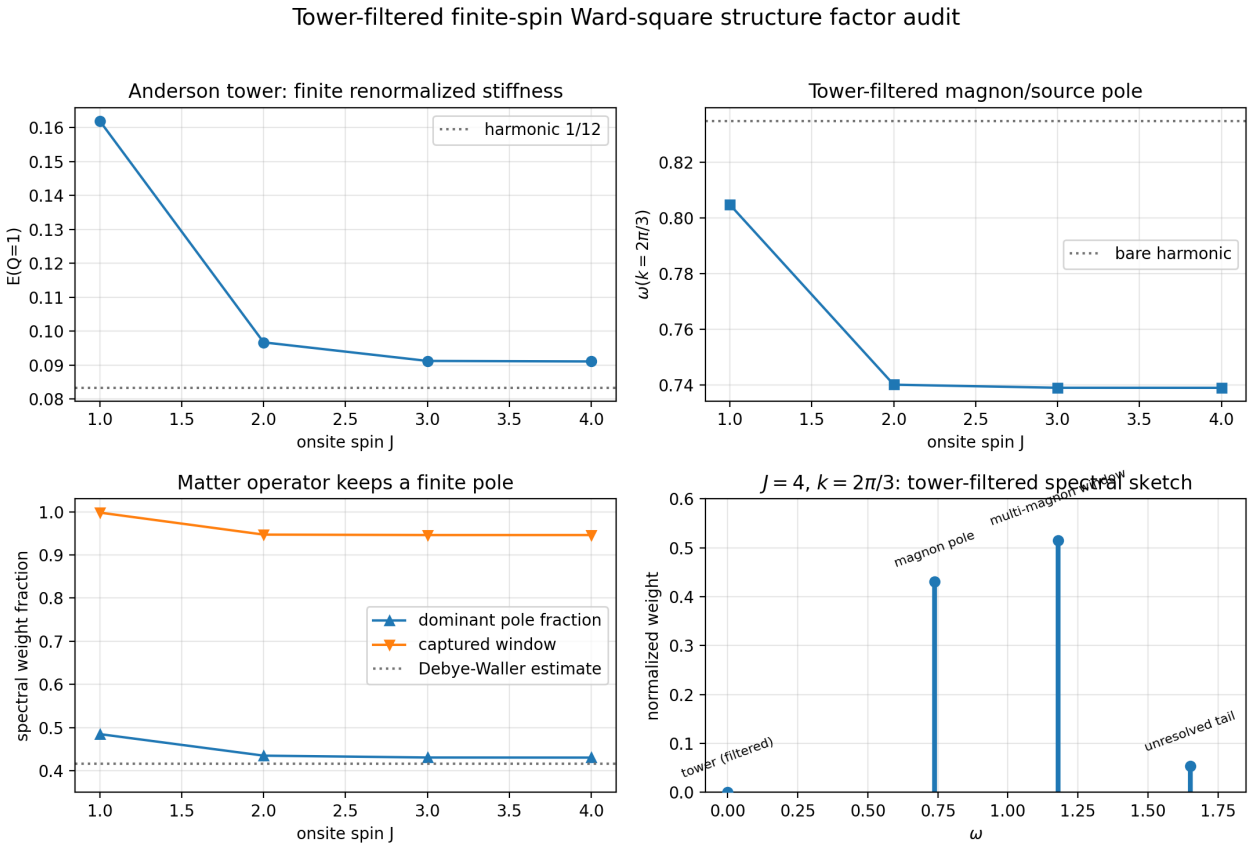

Figure 20: Tower-filtered finite-spin structure-factor audit. The zero-momentum Anderson tower and finite-momentum source pole are distinct. At $k = 2\pi/3$, the tower is filtered out by momentum and the dominant source line remains a finite pole.

This is the first finite-dimensional quantum Hamiltonian check of the compact Ward-square mechanism with an explicit tower-filtered spectral observable. It does not prove the full three-dimensional thermodynamic finite-spin phase: it is a one-dimensional ring, one polarization, small J, and a minimal matter/tensor chain. But it validates the qualitative and quantitative predictions available to that box: Goldstone tower, propagating magnon, and finite matter pole residue after tower filtering.

18 Updated interpretation

The project now has a stronger status than the v3 carrier paper. The effective continuous-variable chiral carrier and Ward-completed square remain the clean analytic core, but the compact route is no longer only a spin-wave extrapolation. It has passed diagonal 3D XY ordering checks, full tensor/matter compact screens, hard-constrained spectral checks, finite-spin saturation estimates, hard quotient compact screens, and a finite-dimensional quantum-box exact diagonalization.

The honest status is therefore

Exact CV chiral Gaussian/QCA spin-2 response carrier: achieved.
Ward-completed dynamical matter square at effective CV/Gaussian level: achieved.
Local covariant seagull localization through $R = S - \alpha A$ constraints: achieved at harmonic level.
Full hard-constrained tensor/matter symbol with $N_{\mathrm{low}}^{\mathrm{TT}} = 2$ and $\chi_S \sim k^{-2}$: *achieved.*
Compact ordered-sector screens and finite-spin saturation control: positive.
Finite-spin compact quantum box with tower, magnon, and source pole: positive.
Theorem-level nonperturbative 3D finite-d graviton phase proof: not yet achieved.

(138)

The remaining distance is no longer a vague mechanism gap. It is a specific thermodynamic finite-spin gauge-Hamiltonian problem: scale the now-explicit tower-filtered structure factor from the quantum box to the full compact tensor/matter Ward-square model and show exactly two TT branches with $z = 1$ and finite Ward-stress residue, with no extra Goldstones or mirror cones.

19 Next calculations

The next calculation should not introduce a new architecture. The architecture is now concrete. The next task is to scale and filter the microscopic finite-spin dynamics:

1. **Thermodynamic tower-filtered spectral scaling.** The $L = 3$ box now has an explicit tower-filtered $S_{SS}(k, \omega)$. The next target is to scale the same observable to larger L, larger synthetic chains, or a transfer-matrix/QMC estimator, while maintaining a finite pole fraction and no extra low line beyond tower plus magnon.

2. **Full microscopic gauge-generator implementation.** Promote the hard quotient used in the spectral screens into local finite-spin gauge generators in the Hilbert space and verify operator-level first-class closure before reduction.

3. **Full two-polarization hard quotient.** Repeat the quantum-box analysis with both TT polarizations and the full hard local constraint structure, rather than a reduced one-polarization chain.

4. **Nonperturbative defect audit in the full model.** Measure compact defects, bounded-flux saturation, and anisotropy-induced mass terms in the same ensemble used for the spectral function.

5. **Finite-spin theorem extraction.** Formalize a conditional theorem: if the compact Ward-square model has an ordered diagonal $U(1)$ sector with finite stiffness, the hard local constraints remain deconfined, and the second hard-quotient gap remains finite, then the tower-filtered TT response has $z = 1$ and $\chi_S(0, k) \sim k^{-2}$.

20 Conclusion

The construction has evolved from a signed single-cone carrier into a compact finite-spin phase candidate with a finite-dimensional quantum-box validation. The central mechanism is now clear. Locality forbids a low-order standalone TT operator and a lone periodic cone; the construction responds by gauging identities rather than inserting forbidden projectors. The cone-doubling debt is paid by a domain wall. The seagull debt is paid by the local covariant difference $R = S - \alpha A$ with local divergence and trace constraints. The mass debt is paid by a diagonal Ward/Goldstone shift. The finite-dimensional canonical-pair debt is paid by a compact ordered rotor/spin sector rather than by exact finite onsite CCR.

The current strongest claim is therefore: a local first-class chiral bosonic spin-2 carrier with a Ward-completed matter square has a compact finite-spin route whose hard-constrained harmonic target, compact ordered screens, finite-spin saturation bounds, and small quantum-box exact diagonalization all support exactly two TT branches, $z = 1$, finite source residue, and $\chi_S(0, k) \sim k^{-2}$. The claim remains below full emergent gravity and below a theorem-level finite-d phase proof. The decisive remaining test is the thermodynamic finite-spin spectral function of the full compact Ward-square tensor/matter model, using the tower-filtered observable now validated in the quantum box.

A Latest audit summary

Table 6: Latest compact finite-spin and hard-constraint diagnostics.

Diagnostic	Value
Full tensor/matter constrained dimension at $W = 16$	$34 = 2W + 2$
Full tensor/matter branch exponents	0.999999525, 0.999999518
Full tensor/matter response exponents	−1.997024224, −1.997024228
Hard-constrained scalar exponent	0.999493439
Hard-constrained response exponent	−1.998965499
Hard-constrained IR residue	0.058823546
Target residue $1/(W + 1)$	0.058823529
Hard BZ extra zeros on 13^3 grid	0
Hard quotient compact screen, $L = 8, W = 4$, $\lvert m\rvert$	0.958911
Hard quotient compact screen, helicity	1.119222
Hard quotient compact screen, vortex fraction	0
Ordered-sector $\bar{n}_{\max,\infty}$	0.020757175
$J = 8$ HP defect estimate	2.595×10^{-3}
$J = 64$ HP defect estimate	3.243×10^{-4}

Table 7: Finite-spin compact quantum-box exact diagonalization.

Quantity	$J = 1$	$J = 2$	$J = 3$	$J = 4$
$E_{Q=1}$ tower gap	0.161944	0.096723	0.091255	0.0911
$\omega(k = 2\pi/3)$	0.80484	0.74001	0.73890	0.73888
Matter pole fraction	0.4850	0.4351	0.4308	0.4306

B Numerical audit summary

Table 8: Chiral bosonic lift parameters.

Parameter	Value
r_0	0.42
r_β	2.5
c_{top}	2.0
Surface width W_{surface}	48
Scan width W_{scan}	32
First-class test width W_{FC}	8
QCA timestep τ	0.25

Table 9: Finite-dimensional truncation diagnostics.

Diagnostic	Value
Largest covariance box L	24
Covariance width W	16
Max $\langle q_s^2 \rangle$ at $L = 24$	0.397764924326
Max $\langle p_s^2 \rangle$ at $L = 24$	1.219767160624
Max $\bar{n}_s$ at $L = 24$	0.167701370515
Extrapolated max $\langle q_s^2 \rangle$	0.400151411669
Extrapolated max $\bar{n}_s$	0.170917403179
Optimized thermal ratio η	0.145968795677
d for local tail $< 10^{-6}$	8
d for local tail $< 10^{-8}$	10
d for local tail $< 10^{-10}$	12

C Companion internal reports

This manuscript is based on the following internal reproducibility artifacts in the same workstream, including the v4 updates:

- Chiral bosonic QCA lift, finite-dimensional truncation, qudit oscillator, and code-protection audits.
- Source-response, mass-protection, approximation-law, local matter/Ward, dynamic matter backreaction, and Ward-completed matter audits.
- Finite-spin Ward-square, compact rotor phase, Ward-stress Gauss-law, tensor seagull, covariant Ward-square, and doubly-constrained compact phase audits.
- Full compact tensor/matter, full compact Monte Carlo phase, finite-spin flux saturation, hard-constraint spectral, finite-spin spectral, hard-constrained compact spin, and microscopic finite-spin ED audits.
- Small-volume quantum-box exact diagonalization scripts and results.

References

[1] H. B. Nielsen and M. Ninomiya, *Absence of neutrinos on a lattice. I. Proof by homotopy theory*, Nuclear Physics B 185, 20–40 (1981).

[2] M. Campostrini, M. Hasenbusch, A. Pelissetto, P. Rossi, and E. Vicari, *Critical behavior of the three-dimensional XY universality class*, Physical Review B 63, 214503 (2001).

[3] QATNU workstream, *Chiral bosonic QCA lift audit*, internal reproducibility report and bundle, June 2026.

[4] QATNU workstream, *Gauged/Ward-completed dynamic matter audit*, internal reproducibility report and bundle, June 2026.

[5] QATNU workstream, *Finite-spin Ward-square audit*, internal reproducibility report and bundle, July 2026.

[6] QATNU workstream, *Compact rotor phase audit*, internal reproducibility report and bundle, July 2026.

[7] QATNU workstream, *Ward-stress Gauss-law audit*, internal reproducibility report and bundle, July 2026.

[8] QATNU workstream, *Tensor quotient seagull locality audit*, internal reproducibility report and bundle, July 2026.

[9] QATNU workstream, *Covariant Ward-square audit*, internal reproducibility report and bundle, July 2026.

[10] QATNU workstream, *Full compact tensor/matter Ward-square audit*, internal reproducibility report and bundle, July 2026.

[11] QATNU workstream, *Hard-constrained spectral audit*, internal reproducibility report and bundle, July 2026.

[12] QATNU workstream, *Small-volume quantum box exact diagonalization*, internal scripts and result note, July 2026.